Identifying short-term variation of dynamic friction by means of its frequency response function

Cabboi, A.; Woodhouse, J.

DOI
10.1016/j.jsv.2020.115212

Publication date
2020

Document Version
Final published version

Published in
Journal of Sound and Vibration

Journal of Sound and Vibration 472 (2020) 115212

Contents lists available at ScienceDirect

Journal of Sound and Vibration

journal homepage: www.elsevier.com/locate/jsvi

Identifying short-term variation of dynamic friction by means of its frequency response function

A. Cabboi [a,*], J. Woodhouse [b]

[a] Faculty of Civil Engineering and Geosciences, Delft University of Technology, Stevinweg 1, 2628 CN, Delft, Netherlands
[b] Department of Engineering, University of Cambridge, Trumpington Street, Cambridge, CB2 1PZ, UK

ARTICLE INFO

Article history:
Received 14 October 2019
Revised 20 January 2020
Accepted 23 January 2020
Available online 29 January 2020
Handling Editor: Ivana Kovacic

Keywords:
Constitutive friction law
Rate-and-state model
Friction-induced vibration
Squeal
Sliding friction
Contact dynamics

ABSTRACT

A challenging case study of dynamic friction was presented in a previous study (A. Cabboi, J. Woodhouse, Validation of a constitutive law for friction-induced vibration under different wear conditions, Wear 396–397 (2018) 107–125), concerning tests performed with a Polycarbonate pin sliding on a steel disc. Identifying and modelling the frictional frequency response for this system turned out to be rarely possible, since the measurements were affected by significant wear and by intermittent squeal occurrence. To shed light on the observed "capricious" behaviour, an "instantaneous" estimation of the frequency response of dynamic friction was developed, allowing the dynamic friction behaviour to be captured and tracked before, and for few cases during, squeal events. Each "instantaneous" frequency response of dynamic friction was fitted by a rate-and-state model, and variations of the model parameters for different sliding speeds, changing normal forces and at different wear stages were tracked. With direct relevance to squeal predictions, the model parameters identified through the proposed processing and fitting methodology could detect rapid transitions between velocity-strengthening and weakening behaviour. These transitions may occur at different sliding speeds, but they also occur during measurements carried out at a constant sliding speed. Based on the identified model parameters, a first qualitative attempt to predict squeal events by means of rate-and-state models is presented, and shown to give promising correlation with experimental results.

1. Introduction

Friction-induced vibration, such as vehicle brake squeal, is important in many technological sectors, and it is common to try to predict squeal propensity of such engineering systems at the design stage. The traditional approach to the characterisation of the frictional behaviour of sliding surfaces to provide input data for such predictions is, however, deeply flawed. It is based on testing with commercial tribometers, which can only measure the mean coefficient of sliding friction during imposed steady motion [2,3]. Environmental factors such as temperature and humidity may be varied, but the test methodology has two major problems. First, squeal typically occurs at frequencies of hundreds or thousands of Hz, in other words on a millisecond time-scale. But conventional testing has a time-scale of minutes, so that it provides no information about dynamic friction at relevant time-scales. Second, friction tests often exhibit "capricious" behaviour: sliding friction may change significantly on time-scales of

* Corresponding author.
E-mail address: A.Cabboi@tudelft.nl (A. Cabboi).

https://doi.org/10.1016/j.jsv.2020.115212

seconds, much shorter than those associated with typical quasi-steady testing. The resulting lack of repeatability is a commonly-encountered problem [4].

A novel methodology for tackling the first problem has been presented in previous papers [1,5,6]. The aim of the present work is to extend this methodology to tackle the second problem. The new approach to characterising dynamic frictional forces at a contact interface is relevant to any prediction method based on complex eigenvalue analysis to determine a threshold of instability. Not all friction-induced vibration can be studied by this linearised approach, but such methods are by far the most common in the research literature and in industrial design practice. The new approach is based on measuring a "frictional frequency response function" $\beta(\omega)$ (see section 2.1 for more details), which captures the linearised behaviour of friction force in the precise form needed for stability analysis. Starting from a chosen operating point of mean sliding speed and normal load, this frequency response function links small changes in friction force to the corresponding small changes in sliding speed.

The rationale of conventional quasi-steady friction testing relies on an assumption that the friction force is a function of instantaneous sliding speed only, often called a "Stribeck model" of friction. If such a model really applies, then the quantity β is simply a fixed real number which is related directly to the slope of the Stribeck curve at the chosen sliding speed. However, in reality $\beta(\omega)$ can be a complex number which changes with frequency: results previously presented have confirmed that this is indeed the case for most of the material combinations tested [1,5,6]. These results also reveal that dynamic friction often shows complicated dependence on normal load and sliding speed, which is not even hinted at by any results obtainable under quasi-steady conditions.

In a traditional Stribeck model, it is easy to see that the slope β of the Stribeck curve has a direct bearing on the question of stability. If the friction force falls with increasing sliding speed (velocity-weakening behaviour), the linearised model describes a negative damping element, with strength given by the slope of the Stribeck curve. For a single degree-of-freedom oscillator, if this negative damping overcomes the positive mechanical damping of the oscillator, it will naturally become unstable. More careful studies have shown that this description is naively over-simplified when applied to multi-modal systems such as a brake disc [7,8], but nevertheless the argument has some validity: velocity-weakening friction tends to promote instability [9–11]. In terms of the new quantity $\beta(\omega)$, the corresponding simple idea would suggest that if $\mathrm{Re}(\beta(\omega)) > 0$ in a certain frequency range, then an oscillator with a resonance frequency in that range might be destabilised (see Appendix B for more details). Experimental evidence to support this idea will be shown in section 4.

The published results for $\beta(\omega)$ have one thing in common with conventional quasi-steady friction tests: they only resolved any time variation of the frictional behaviour on a time-scale of minutes, because each measurement used an averaging procedure covering 2 min of recorded data. However, some of these tests showed evidence of the familiar "capricious" nature of friction: intermittently, audible noise was generated by the measurement rig, which for brevity will be described here as "squeal". This squeal, involving frequencies in the kHz range, would come and go over a time-scale of seconds. To investigate this intermittent behaviour, it will be shown in section 2.1 that the procedure for extracting $\beta(\omega)$ from the sensor signals produced by the test rig can be modified to use only 5 s of data, so that any time variation of the dynamic frictional regime during a 1- or 2-min run at a fixed sliding speed and normal force can be tracked on a shorter time-scale.

In order to model the behaviour revealed in the earlier measurements, an enhanced friction model was needed. It was shown that a rate-and-state model gave good fits, provided it was enhanced by including the effect of tangential compliance in the contact region [1,6]. Such a model allows the measurements to be interpreted by extracting values of a small number of parameters, as will be explained in section 2.2. The same model-fitting methodology will be applied to the results to be presented here, to reveal any time variation of the model parameters.

The target of this study is to exploit the above mentioned "instantaneous" estimation of the frequency response of dynamic friction to capture and track the contact dynamic behaviour during different frictional regimes: at the onset and after a squeal event, and during measurements where no squeal event occurred. In particular, the enhanced data processing technique aims to shed some light on the observed "capricious" behaviour observed in the results obtained using a Polycarbonate pin against a steel disc, which turned out to be the most challenging case study [1]. Squeal occurrence, wear, and rise of the mean friction coefficient pushed the modelling of the observed dynamic friction behaviour to its limit. In addition, the previous work [1] has been augmented by a further testing campaign using the same material combination.

Two main results can be anticipated here. First, the identified rate-and-state model parameters will show significant variation for different runs and especially within a single measurement during which squeal events occurred. In order to unpack possible patterns hidden within the observed parameter variation, the variation of each model parameter is first investigated separately in sections 3.3 and 4.1. Subsequently, in section 5 a correlation analysis, an analysis of variance (ANOVA) and a factor analysis have been carried over the whole data set. The combination of these techniques reveals the number of independent drivers for the observed variation.

The second outcome of this study is of direct relevance to squeal prediction. The model parameters identified over a shorter time-scale will highlight rapid transitions between velocity strengthening and weakening behaviour, not only for measurements performed at different velocities (as commonly observed, e.g. Stribeck curves), but also during each individual measurement run carried out at a constant sliding speed. These transitions seem to be well correlated with the appearance of temporary squeal events. This last evidence may provide a new perspective on why squeal events can occasionally occur on a nominal velocity-strengthening branch of the Stribeck curve [12], and a measured example is provided in this paper. A preliminary attempt is also made to check eventual improvements in terms of squeal predictions if a validated dynamic friction law is available. The example provided in this paper refers to a single degree of freedom system, aiming at catching the stability threshold of one particular mode predominantly acting in the sliding direction. Bear in mind that this single mode system should not be taken as

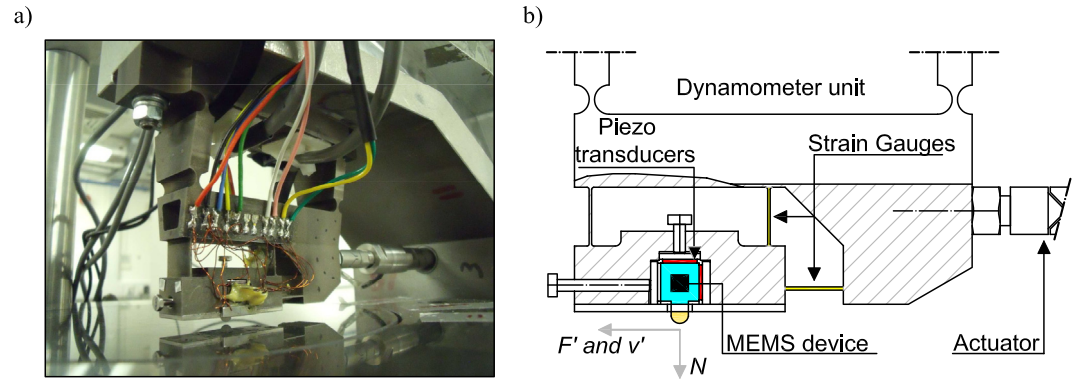

Fig. 1. a) View of the pin-on-disc rig and b) layout of the installed sensors in the dynamometer.

a reference minimal model to predict friction-induced vibration phenomena, since more modes are generally necessary to reach an acceptable predictive convergence [7]. Besides, as already discussed in a previous work [8], the component of modal motion acting normally to the contact surface and the "normal" dynamic friction (not measured yet) are two necessary ingredients for a potential minimal model. Further comments and observations are provided section 4.

2. Measurement, modelling and identification overview

2.1. "Instantaneous" estimation of $\beta(\omega)$

Fig. 1 shows the pin-on-disc test rig, whose technical details and sensor calibration procedure have been thoroughly described in earlier work [5,6]. This rig was specifically developed to provide calibrated interfacial data to support earlier studies based on an idealized model of a single point of contact [7,13]. It is used again here to provide a proof of concept for the proposed enhanced measurement methodology for $\beta(\omega)$ [6]. The approach could be applied to any type of contact, conformal or nonconformal, but is here used in the context of approximate point contact. However, as discussed in earlier work [6], it is a target for future research to develop the measurement technique from a localised frictional contact to a more extended conformal contact.

The signals relevant to estimate the frictional frequency response are obtained from a dynamometer instrumented with strain gauges, and holding a small inner block on which a tri-axial MEMS accelerometer and piezo-electric force transducers are mounted. The tested sample is a hemispherical pin glued to the bottom face of the inner block, which is loaded normally into contact against a rotating disc of the chosen counter-face material. A piezo-electric actuator allows small computer-controlled perturbations of sliding speed to be superimposed.

The test rig has been designed to measure the frequency response of dynamic friction up to mid-high frequency (4 kHz) during steady-sliding contact for different normal forces, sliding speeds and material pairs. Suppose that the steady-state sliding speed v_0 is modulated by a small oscillatory perturbation

$$v \approx v_0 - v' e^{i\omega t}. \tag{1}$$

If $|v'| \ll v_0$ so that linear theory is applicable, the dynamic frictional force must take the form:

$$F \approx F_0 + F' e^{i\omega t}. \tag{2}$$

The frequency response of dynamic friction is then defined as the ratio of the two perturbative quantities:

$$\beta(\omega) = \frac{F'(\omega)}{v'(\omega)}. \tag{3}$$

In general $\beta(\omega)$ will be complex, representing a phase difference between the force and velocity perturbations. It encapsulates the minimal friction information necessary for any linearised stability analysis for systems in sliding contact. Once the dynamic friction force and tangential velocity fluctuations have been measured, the H_1 estimator [14] is used to compute the frequency response function.

In previous work [1,5,6], each $\beta(\omega)$ function was estimated using 120 s of measured data sampled at 20 kHz, averaging the auto/cross-spectral densities of 120 1-s segments in order to provide a stable estimate, together with the associated coherence function as a check for linearity. In more recent tests (September 2018), to be compared to the earlier results (March 2016) in this paper, each single measurement was shortened to 60 s. The two datasets will be called "Set 1" and "Set 2" in the following discussion. The approach of computing $\beta(\omega)$ over a 1 or 2 min run turned out to be satisfactory and reliable for material pairs not prone to wear (e.g. Nylon/glass, Polycarbonate/glass, Perspex/glass, Tufnol/glass [1]. It should be noted that the material pairs tested in the previous study [1] were not motivated by specific engineering applications, but chosen to provide a wide-ranging

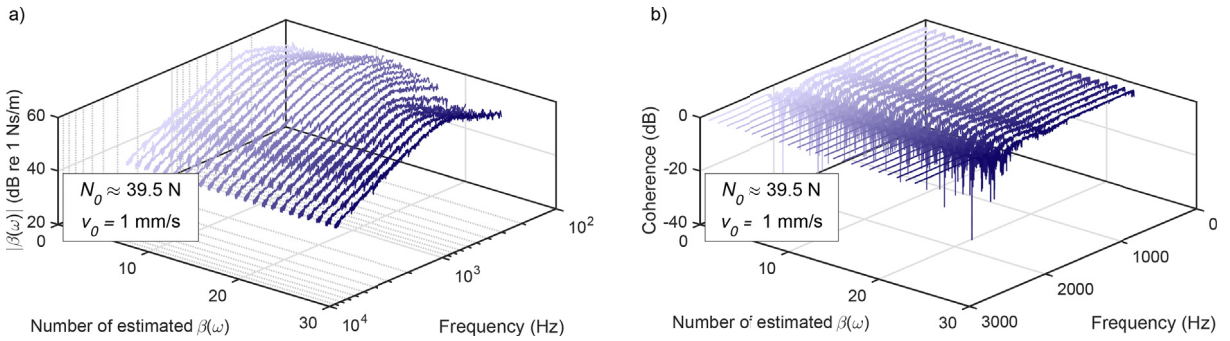

Fig. 2. (a) Estimates of $|\beta(\omega)|$ every 5 s over a measurement length of 120 s carried out at a disc speed of 1 mm/s and an approximately stable normal force around 35.5 N; (b) corresponding coherence function.

proof of concept for the measurement and interpretation of $\beta(\omega)$. In particular, Polycarbonate was chosen for its good thermal stability, making it reliable and convenient for friction testing.

However, improvements seemed to be necessary for the Polycarbonate/steel case, for two reasons. First, effects of rapid wear were observed: the hemispherical-shaped Polycarbonate pin sample started the testing sequence with a non-conformal contact and ended with a conformal contact with a radius of the order of 1 mm (see Fig. 13 of [1]). The second issue was that the Polycarbonate/steel combination often exhibited intermittent squeal in the test rig, invalidating the measurement procedure based on long-time averaging. This case is the focus of the present work. In order to tackle the issue of time variation, an "instantaneous" $\beta(\omega)$ function has been estimated every 5 s, with each estimate involving an average over five 1-s segments. The new estimation technique has been applied to the Polycarbonate-steel results from Set 1 and Set 2.

Fig. 2a provides a first example of how this new instantaneous $\beta(\omega)$ function can change over the course of one single measurement period (in this case over 2 min). A logarithmic frequency scale and a slightly odd viewing angle have been chosen, to show the data and its variability to best advantage. The plots shows significant changes in $\beta(\omega)$ occurring in the low frequency range (up to 1 kHz), while a remarkable repeatability is found at higher frequencies. Even with so few averages, the coherence, shown in Fig. 2b, was generally found to be good apart from a reduction around 2 kHz. As explained previously [5,6], this reduction is due to the input excitation, which was deliberately reduced over that specific frequency range in order to avoid a resonance of the dynamometer unit.

For both data sets, different subsets of measurements were made, each with a different level of normal force ranging approximately between 10 N and 40 N. The measurements for each subset involved a sequence of sliding speeds, increasing and then decreasing in the pattern 1, 2, 4, 6, 8, 10, 10, 8, 6, 4, 2, 1 mm/s. The investigated frequency range of each measurement was 0.1–3 kHz, sampled at 20 kHz (note that the induced excitation goes up to 4 kHz).

2.2. Modelling and parameter identification

It has been shown previously that the measured $\beta(\omega)$ functions for different velocities, normal forces and frequencies can be accurately approximated by a dynamic friction model that combines a phenomenological rate-and-state model of the Dieterich-Ruina type [1,6] with allowance for tangential contact stiffness. In a parallel development, the idea of allowing for tangential compliance to enhance the prediction performance of rate-and-state models has also been recently pursued within the geomechanics community [15,16]. The basic Dieterich-Ruina model to be used in this paper [17,18] defines the friction force F as

$$F = N_0\mu = N_0[\mu_* + a\ \ln(v/v_*) + b\ \ln(\phi/\phi_*)] \tag{4}$$

where N_0 is the steady-state normal force, μ is the classical Coulomb coefficient of friction, v defines the slip velocity, ϕ is an internal state variable, subscripts "$*$" indicate chosen reference values, and a and b are dimensionless model parameters. This equation describes behaviour which is monotonic with v. A more general non-monotonic friction model has also been discussed in previous work [6,19], but the current experimental methodology is not mature enough to reliably identify all the model parameters of a non-monotonic model.

Equation (4) is coupled with a state evolution law [20], that reads

$$\frac{\mathrm{d}\phi}{\mathrm{d}t} = -\frac{\phi - \phi_{ss}(v,\ldots)}{t_\phi(v,\ldots)} \tag{5}$$

where the subscript ss denotes the steady-sliding value. The time-scale parameter t_ϕ can be taken as a fixed constant, or could be dependent on velocity through the standard length-scale parameter L [6]. The state variable ϕ in Eq. (5) captures memory effects in response to variations of the slip velocity. Under conditions of steady sliding, the Dieterich-Ruina model reads

$$F_{ss}(v_0) = N_0[\mu_* + (a-b)\ \ln(v/v_*)]. \tag{6}$$

Equation (6) describes a logarithmic dependence on the slip velocity, and the term $(a-b)$ characterises the slope of the F_{ss} – v_0 curve. If $(a-b)$ is positive, the friction curve shows velocity-strengthening behaviour, while velocity-weakening behaviour occurs with a negative sign of $(a-b)$. A frequency response of dynamic friction can be recovered from Eqs. (4) and (5) by perturbing the variables v and ϕ and linearising in the frequency domain around a chosen operating point. Following the sign convention from previous works [5,6], the rate-and-state model assumes the following expression

$$\beta_{RS}(\omega) = -\frac{[g_{,\phi}^2 f'_{ss} + \omega^2 f_{,v}] + i\omega g_{,\phi}[f_{,v} - f'_{ss}]}{g_{,\phi}^2 + \omega^2}. \tag{7}$$

where

$$f'_{ss} = \mu'_{ss} N_0 = \frac{(a-b)N_0}{v_0}; \quad f_{,v} = \mu_{,v} N_0 = \frac{aN_0}{v_0}; \quad g_{,\phi} = \frac{1}{t_\phi} \equiv \frac{L}{v_0}. \tag{8}$$

The symbols f and g refer respectively to the friction law in Eq. (4) and the state evolution law in Eq. (5).

As discussed in the earlier work [6], the tangential stiffness, necessary to reproduce the measured $\beta(\omega)$, involves a series combination of the pin's tangential bulk stiffness and an interfacial contact stiffness from the effect of asperities. It was not possible to identify these contributions separately from any individual measurement, although some progress was reported by analysing a matrix of data obtained under different operational conditions. For the present purpose, the new instantaneous measurement is always based on a single test so that it is only possible to obtain a single effective stiffness k_t.

In order to capture the measurement of $\beta(\omega)$ presented in this paper, we assume that the contact stiffness k_t is coupled in series with the dynamic friction $\beta_{RS}(\omega)$, leading to an "equivalent" compliant pin model $\beta_{CP}(\omega)$ [6]:

$$\beta_{CP}(\omega) = \beta_{RS}(\omega) \times \frac{1}{1 - i\omega\beta_{RS}(\omega)/k_t} \tag{9}$$

The model parameters of the rate-and-state model that need to be identified in combination with the tangential stiffness k_t are a, b and L (or t_ϕ). The best fit between the chosen model and the $\beta(\omega)$ measurements is obtained by minimising the cost function

$$\min_{\Phi} \ \epsilon(\omega, \Phi) = \min_{\Phi} \sum_{\omega=\omega_{min}}^{\omega_{max}} |\beta^{exp}(\omega) - \beta_{CP}(\omega, \Phi)|^2 \tag{10}$$

which is simply the squared difference between the experimental data $\beta^{exp}(\omega)$ for a specific normal force and sliding speed and the corresponding model $\beta_{CP}(\omega, \Phi)$. The vector Φ contains the fitting parameters. The minimisation is performed using the Matlab routine *"fminsearch"*.

Fig. 3a and b shows two examples of measurements with corresponding model fits, shown as Nyquist plots in the complex plane over the frequency range 0.1–3 kHz. The corresponding identified model parameters are also given. Both plots were characterised by excellent coherence, and refer to measurements where no squeal occurred. By inspecting the sign of $(a-b)$, it can be noted that Fig. 3a shows a dynamic friction function corresponding to velocity strengthening behaviour, while Fig. 3b corresponds to velocity weakening. This distinction can also be inferred directly from the plots, since for negative values of $(a-b)$ the Nyquist curve crosses to the right complex half-plane at low frequencies. Fig. 3c shows an example of $\beta(\omega)$ estimated immediately before a squeal event. The level of noise in the measurement is obviously higher, but the shape of $\beta(\omega)$ in the complex plane still resembles a segment of a circle, and the corresponding fitted model parameters still fall within a reasonable range of numbers. On the other hand, Fig. 3d shows very unsatisfactory results for $\beta(\omega)$ estimated during a squeal event. Any attempt at model fitting in such a case is doomed to failure, and such results were systematically discarded.

2.3. Literature on rate-and-state model parameters

In previous literature, the values of fitted model parameters a, b and L are often reported in tables through mean values and, in the best case scenario, with corresponding standard deviations. These rate-and-state model parameters are usually retrieved from typical quasi-static geomechanical laboratory tests such as velocity-step tests [17,21], slide-hold-slide tests [21] and sliding tests [22]. On the other hand, the identification of such parameters from dynamic friction tests performed at mid-high frequencies was made possible only recently [1,6]. Once these parameters are identified and selected, they are commonly used as time-constant input parameters for numerical modelling investigations [23]. Such an approach would be justified if the tested material combination were not much affected by wear. In previous studies [1,6], runs carried out at different sliding speeds and normal forces for materials such as Nylon/glass or Polycarbonate/glass, a single set of model parameters could remarkably fit most of the experimental results. However, according to the results to be presented here it seems quite implausible that these parameters should be treated as time-constant values if wear becomes non-negligible. Dependencies of rate-and-state model parameters on operational conditions such as (and not limited to) temperature [24–28] and normal stress [29,30] have been commonly reported in the literature, corroborating the idea that these model parameters may be only representative of a specific contact configuration [31].

Robust prediction of propensity to squeal surely requires that variability of such model parameters be taken into account. If the influence of operational conditions and wear on these model parameters is not negligible, large fluctuations of the kind

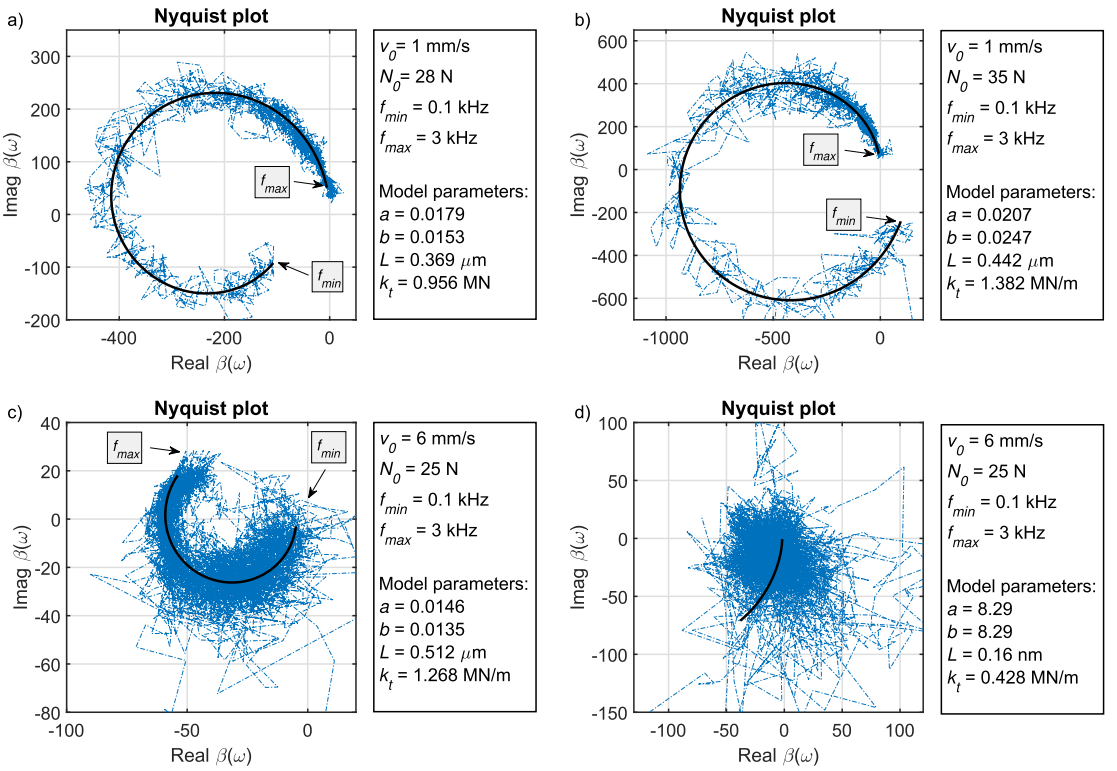

Fig. 3. Nyquist plots of $\beta(\omega)$ estimated for a 5 s time segment: (a) measurement carried out with disc speed 1 mm/s and normal force 28 N; (b) measurement carried out with disc speed 1 mm/s and normal force 35 N; (c) measurement carried out at the onset of a squeal event with disc speed 6 mm/s and normal force 25 N; (d) measurement carried out during the ensuing squeal event with disc speed 6 mm/s and normal force 25 N.

to be presented here are inevitable and a single set of model parameters would not be able to capture the observed frictional behaviour. A promising approach to tackle this problem has been laid down in the last two decades, based on a microphysical derivation for the rate-and-state model parameters [20,32–36]. Detailed discussion of these microphysical models falls outside the scope of this paper, but some relevant outcomes will be briefly discussed in subsection 4.1 in order to try to shed light on the observed frictional behaviour reported here.

3. Identified model parameters for polycarbonate pin on steel disc

3.1. Summary of estimated quantities and testing procedure

From each single measurement several quantities were estimated. The mean kinetic coefficient of friction μ_k was obtained by averaging the tangential and normal forces measured by the strain gauges over each full measurement (120 s for Set 1, 60 s for Set 2). In addition, an "instantaneous" kinetic coefficient of friction $\mu_{k,I}$ and the "instantaneous" function $\beta(\omega)$ were estimated for every 5 s of recorded data. Section 3.2 gives a discussion of the behaviour and variability of the estimated coefficient of friction. The remaining subsections focus on the variability of $\beta(\omega)$ and the corresponding fitted model parameters.

As will shortly become evident, some common patterns and some significant differences were found between the two data sets. Each set began with a new Polycarbonate pin sample, nominally identical. Two years had elapsed between the two experimental campaigns, and meanwhile other tests were performed on the same steel disc, near to the chosen operating radius. This could have led to differences in the topography and chemistry of the disc surface, including any transferred film of wear debris from other tests.

The pattern of the tests was somewhat different for the two data sets. Each data set was recorded over three days of testing. For Set 1, three subsets were recorded, each being measured on a different day so that the apparatus was left overnight. This will have allowed an opportunity for everything to cool down to ambient temperature, and perhaps for some oxidation processes to operate on the pin and transfer film. Set 2, on the other hand, contains seven subsets. The first four were measured in close succession during the first day, the fifth and sixth on the second day after an overnight pause, and the last subset was recorded on the third day after another overnight pause. The extra subsets in Set 2 were designed to enlarge the database, including some repetition of nominal operating conditions, and cases with the pin in conformal contact due to wear after the more extensive testing.

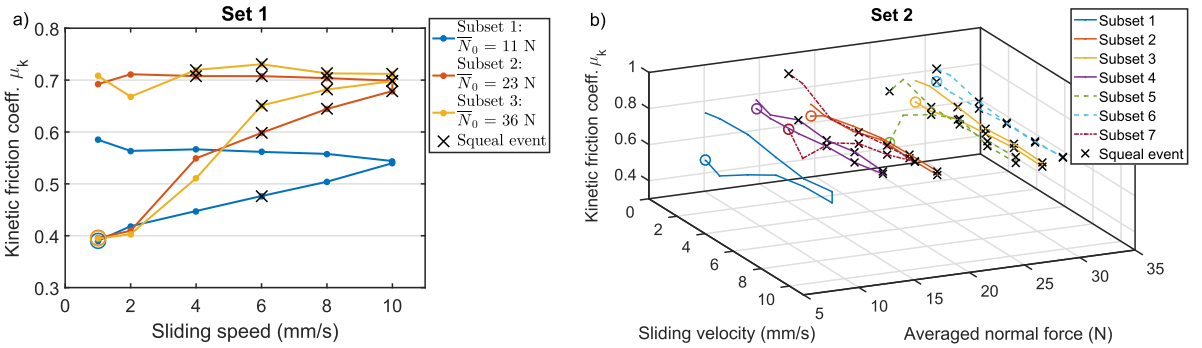

Fig. 4. Estimated kinetic friction versus sliding speed for Set 1 (a) and Set 2 (b). The cross marker highlights squeal occurrence and the circles indicate the starting point for each subset of measurements.

3.2. Estimated friction coefficient μ_k and squeal events

Fig. 4a and b shows all the estimated $\mu_k - v_0$ curves for Set 1 and Set 2. The circles in Fig. 4a and b indicate the first run for each subset of data. Each subset was labelled with the mean normal force $\overline{N}_0$, obtained by averaging over 12 runs at different sliding speeds: increasing and then decreasing through the same values. As already mentioned, these tests sometimes exhibited friction-induced instability: the black crosses in Fig. 4 mark the runs during which squeal was heard.

Set 1 shows a pattern that seems quite simple and intuitive. The initial branch of each curve, as sliding speed was increased 1–10 mm/s, shows increasing friction force with time and/or increasing sliding speed. The result resembles typical velocity-strengthening behaviour in a Stribeck curve [2]. However, the first and second branches of the $\mu_k - v_0$ curves do not agree: the friction coefficient remains high as sliding speed decreases. Subsets 2 and 3 show a striking level of agreement, suggesting independence of normal force following the familiar Amontons-Coulomb 'law' for the coefficient of friction. This feature was already seen in previous work [1]. Subset 1 is different, but the first subsets of any such data set might be expected to show running-in behaviour of some kind, as is familiar for first runs of friction tests [4]. A feature that jumps immediately to the eye is the remarkably similar initial values of μ_k for all three subsets. As mentioned earlier, each subset of Set 1 was recorded at a different day. This will have allowed the apparatus to cool down: a full testing sequence (subset) generates significant friction heating. Processes such as oxidation will also have had a chance to operate, changing the surface chemistry during a few quiescent hours.

The results for Set 2 share some common features, but there are also significant differences. The plot, Fig. 4b, has been presented in 3D form in the hope for greater clarity: a 2D plot similar to Fig. 4a is difficult to decode because there are more curves and also because most of the data points seem to be confined to a narrow range between 0.7 and 0.9. The first branch of most curves again shows increasing friction force, except that some subsets show an initial decrease between the first two sliding speeds. The second branch generally does not follow the same track, but subset 2 and 4 are two exceptions. All the curves apart from subsets 2 and 4 show a clear increase of the coefficient of friction between the first run and the last run, as did all the curves in Set 1. This rise of the friction force can probably be attributed to an increase of the surface temperature, and perhaps to a changing state of the surface chemistry of pin and disc during extended testing.

The initial values (circled in the plot) do not show the same repeatability as was seen with Set 1. However, the three cases run after a night's rest (subsets 1, 5 and 7) all show relatively low initial values of μ_k, and those for subsets 1 and 5 are very similar. None shows an initial value of μ_k as low as those seen for Set 1. The comparison between subsets 1 and 4 of Set 2 is worth noting: these have similar normal loads, but the tests were performed at the beginning and the end of the test sequence on the first day. There is no obvious trace of similar behaviour between these two subsets.

The pattern of squeal events in the two data sets can also be compared. Squealing typically occurred intermittently at a variety of mid-high frequencies, and in a few cases at a sliding speed of 1 mm/s even steadily at lower frequencies. The first runs, generally obtained at a normal force close to 10 N, were not prone to squeal events, while the last runs carried out at higher normal forces exhibited squeal events in all subsets. The first squeal event always occurs in the first branch of the $\mu_k - v_0$ curve, which always shows a velocity strengthening regime. This observation may seem unexpected since friction-induced instability phenomena are historically linked to velocity-weakening behaviour of the friction force [9]. Section 4 will shed some light on this counter-intuitive observation by inspecting the short-term variation of the friction force - velocity slope through "instantaneous" estimates of $\beta(\omega)$. In general, the squeal events mostly occurred at sliding speeds of 6, 8 and 10 mm/s for normal forces higher than 10 N. On the other hand, for the runs performed with a mean normal force close to 10 N only one squealing event was observed, at a sliding speed of 6 mm/s, see Fig. 4a. Some squeal events were also detected in tests performed at 4 mm/s and even at 1 mm/s. Curiously, no squeal was ever detected for any of the tests carried out at a sliding speed of 2 mm/s in either test set.

"Instantaneous" estimates of the kinetic coefficient of friction were also made over each 5 s interval during each test. The goal was to detect possible patterns caused by short-time variation within each measurement. Fig. 5a and b shows examples of such

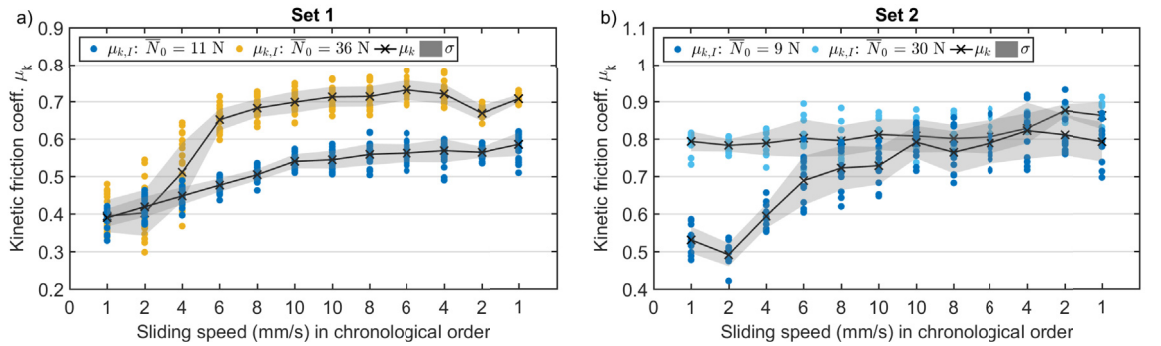

Fig. 5. Selected test sequences showing estimates of the instantaneous kinetic friction, $\mu_{k,I}$, versus sliding speed displayed in a chronological testing order for Set 1 (a) and Set 2 (b). The black lines refer to the estimes of μ_k, while the shaded grey area delimits the uncertainty bound quantified by means of the standard deviation.

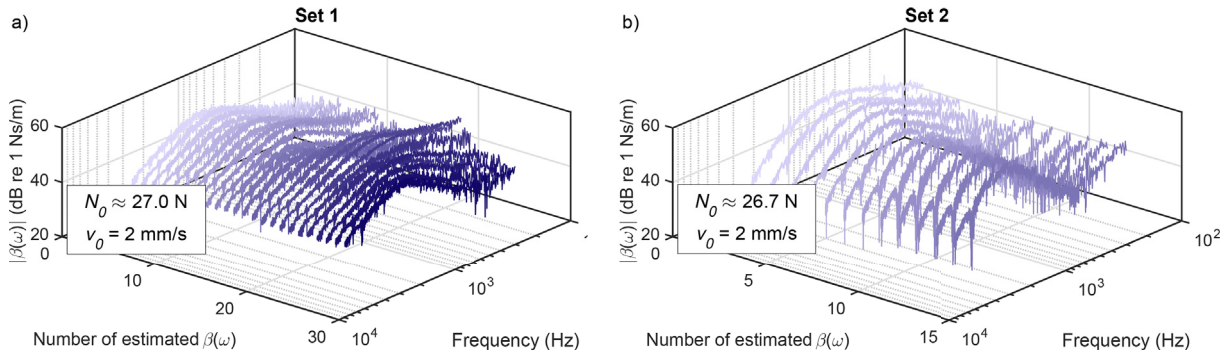

Fig. 6. Estimates of $|\beta(\omega)|$ every 5 s over a measurement length of 120 s from Set 1 (a) and 60 s from Set 2 (b). Both plots contain measurements carried out at a disc speed of 2 mm/s and an approximately stable normal force around 27 N.

estimates, for subsets 1 and 3 of Set 1 and of Set 2. The black lines show the corresponding estimates of μ_k from Fig. 4, while the discrete points show the individual samples within each measurement, and the shaded grey area gives the uncertainty bounds quantified through the standard deviation of these samples. Within each measurement, the quantity $\mu_{k,I}$ seems to fluctuate randomly without any distinctive time variation pattern. Somewhat counter-intuitively, Fig. 5a exhibits the highest variability for measurements performed at lower speeds during the last test sequence carried out at $\overline{N}_0 = 36$ N. On the other hand, Fig. 5b shows higher variability for the first test sequence performed at $\overline{N}_0 = 9$ N, more in line with expectations. It was interesting to observe that for the measurements during which squeal occurred, no significant change of the variability of $\mu_{k,I}$ was observed.

3.3. Identified rate-and-state model parameters from $\beta(\omega)$

The $\mu_k - v_0$ results from the previous section show rather complicated behaviour with no clear patterns and little evidence of repeatability. These measurements, similar to traditional tribological tests, do not seem to shed clear light on the occurrence of squeal or on the observed variations and anomalies. However, as earlier work [5,6] has stressed, the function $\beta(\omega)$ may provide a clearer fingerprint of dynamic friction than anything deduced from the coefficient of friction. Fig. 4 suggested that the results from Set 1 and Set 2 behaved in different ways. For an initial indication of whether the same is true for the instantaneous $\beta(\omega)$ functions, Fig. 6 shows a comparison of approximately corresponding runs from Set 1 (Fig. 6a) and Set 2 (Fig. 6b): the $\beta(\omega)$ functions in both plots were estimated at the same sliding speed and at a fairly similar normal force. The general shape with changing frequency is quite similar, and, as anticipated in Fig. 2a, both plots show significant variability at lower frequencies but strong repeatability at higher frequencies. However, systematic differences in shape can be seen between the two cases, a question to be explored in more detail in section 5.

The compliant pin model of Eq. (9) has been systematically fitted to the estimates of the instantaneous $\beta(\omega)$ functions, wherever the data quality permitted a satisfactory analysis (see Fig. 3). This fitting process gives time-varying values for the parameters a, b and L of the friction model, and also for the tangential contact stiffness k_t. Recall that the constitutive friction law dominates the $\beta(\omega)$ behaviour of this model at low frequency, whereas the tangential contact stiffness becomes important at higher frequency. The behaviour seen in Fig. 6 thus leads one to expect relatively small variability of k_t and higher variability for the friction parameters. Fig. 7 confirms this predicted trend. For both data sets, the raw plotted data and also the coefficient of variation (reported in the legend) show that parameter L exhibits the largest variability, followed by parameters b and a. On

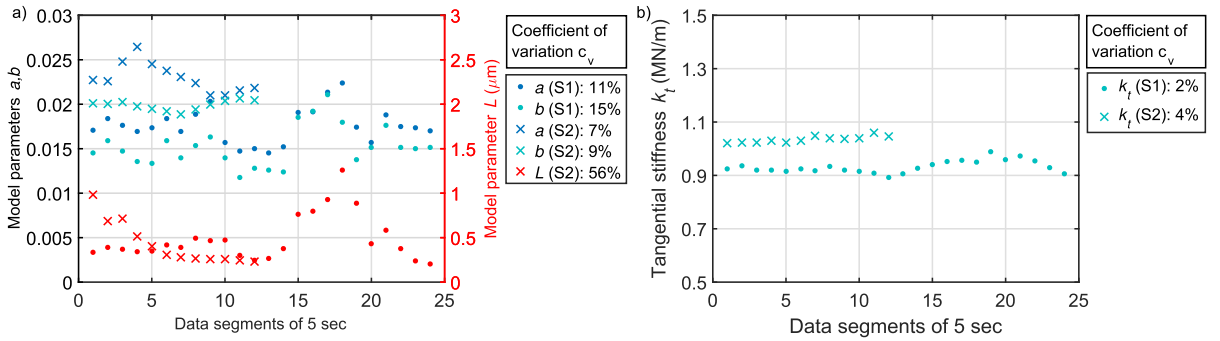

Fig. 7. Fitted model parameters for Set 1 and Set 2 corresponding to the $\beta(\omega)$ functions plotted in Fig. 6: (a) parameters a, b and L; (b) parameter k_t.

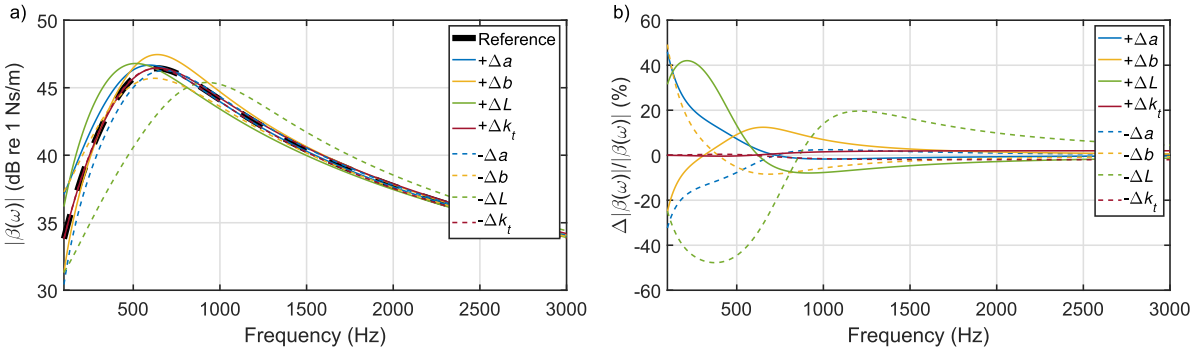

Fig. 8. (a) Changes of the magnitude of $\beta(\omega)$ induced by perturbing each parameter separately by the estimated variability shown in Fig. 7 for Set 1; (b) percentage variation of $\beta(\omega)$. The following model parameters were used for the reference case: $v_0 = 2$ mm/s, $N_0 = 27$ N, $a = 0.0176$, $b = 0.0152$, $L = 0.48$ μ and $k_t = 0.93$ MN/m.

the other hand, the tangential stiffness remains essentially constant within each measurement.

Parameter L shows by far the biggest coefficient of variation, but it is important to recall that the sensitivity of $\beta(\omega)$ varies greatly between the different model parameters: see Fig. 12 of [6]. Parameter L shows the lowest sensitivity in general. Fig. 8 illustrates the impact on $\beta(\omega)$ of the estimated variability of each model parameter for the measurement shown in Fig. 6a. A reference case was simulated based on the mean values of the model parameters identified in Fig. 7 for Set 1. The reference case was then perturbed by inducing a change on each model parameter, separately, corresponding to the estimated variability. It can be observed that for an increase of parameters a, b and L, the impact on $\beta(\omega)$ is fairly similar despite the large variability observed for L. On the other hand, for a decreasing perturbation, the change of parameter L shows a more pronounced effect on $\beta(\omega)$. Despite this difference, the general pattern governing which are the dominant parameters at low and high frequency does not change. The analysis in terms of coefficient of variation has been applied to each measurement of both data sets, and similar trends to those depicted in Fig. 7 were generally observed. The only slight exceptions were Set 1, subset 3 and a few cases in Set 2, where the variability of k_t overlapped with or exceeded that of a and b.

The general trend of each variable following the chronological order of measurements can also be analysed. Fig. 9 shows all the identified values of the tangential contact stiffness from the estimated $\beta(\omega)$ functions, plotted sequentially in the order of testing. Gaps in the sequence indicate the cases where a satisfactory model fit was not possible. Regions where squeal occurred are also shown. It can be seen that it was only rarely possible to obtain satisfactory model fits within these regions: subset 3 of Set 1 is the main exception, and advantage will be taken of these data points when squeal events are examined in detail in section 4. Wear of the pin is evident in the progressive increase of stiffness as the area of contact increases.

Fig. 10 shows the same stiffness data, plotted against normal force. The chronological order of measurements within each subset is here tracked through colour: the lightest dots refer to the first measurements, progressively darker ones to later measurements. A colour distinction has also been made based on the day of measurement for each subset. In very broad terms, an increase of tangential stiffness can be observed for increasing normal forces. An attempt has been made to estimate the expected order of magnitude of this stiffness, to compare with the fitted values and their trends. Very simple estimates can be made of three types of stiffness that may contribute: see Appendix A for details. These are the bulk shear stiffness of the pin, the tangential Hertzian stiffness which would apply to a non-worn contact, and the stiffness associated with asperities in a rough-surface contact (estimated from the familiar Greenwood-Williamson (GW) model). The measured effective stiffness can be expected to involve a combination of all three factors [37], in proportions that will change as the pin wears.

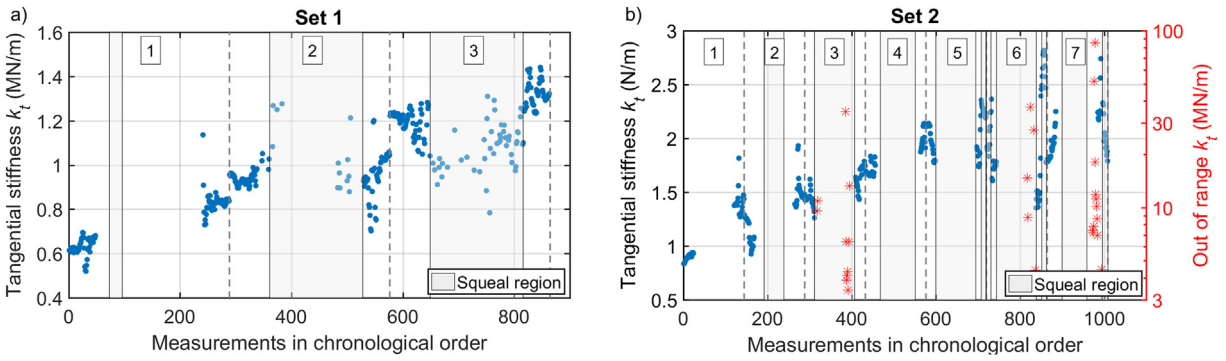

Fig. 9. Plot of the tangential stiffness, k_t, identified from the estimated $\beta(\omega)$ functions following the chronological order of measurements: (a) Set 1; (b) Set 2. The numbers provided in the small boxes identify each subset of data, while the red crosses in (b) highlight potential outliers. (For interpretation of the references to colour in this figure legend, the reader is referred to the Web version of this article.)

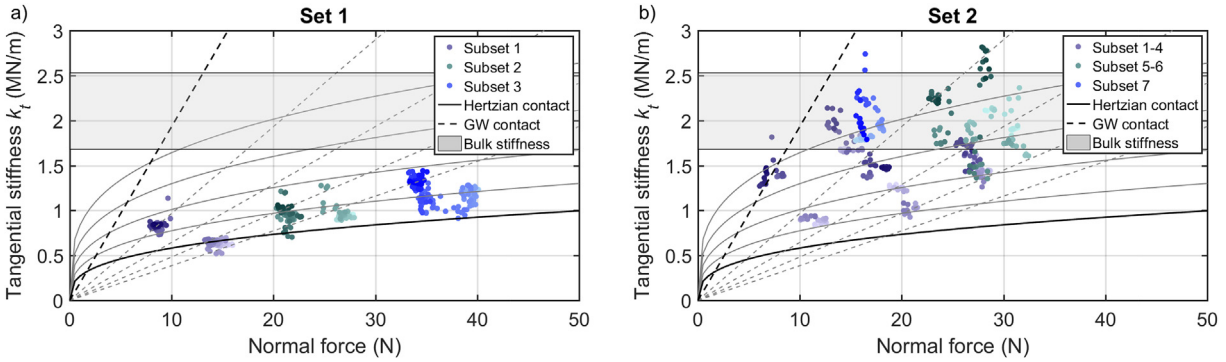

Fig. 10. Identified tangential stiffness, k_t, versus measured normal force N_0: (a) Set 1; (b) Set 2. The colour transition from light to dark follows the chronological order of measurements for each subset. Colours have been used to group the subsets that were tested on the same day. The continuous black line in Fig. 10a shows the expected trend from a Hertzian contact with an exponent of 1/3 (see Eq. (A.2)), and the upper grey curves were obtained by decreasing the exponent from 1/3 to 1/3.4 in steps of 0.01. The varying parameter of the GW contact model is σ (see Eq. (A.3)). The black dashed lines refer to an initial σ value of 0.4×10^{-5}, and the following dashed grey curves were obtained by increasing σ in steps of 0.4×10^{-5}. The grey shaded region indicates the approximate range of the pin's bulk stiffness, calculated according to Eq. (A.1). (For interpretation of the references to colour in this figure legend, the reader is referred to the Web version of this article.)

All three estimated stiffnesses are indicated in Fig. 10. The Hertzian stiffness is computed according to Eq. (A.2), using the measured pin radius $R = 1.5$ mm and elastic properties of Polycarbonate taken from the literature: Young's modulus 2.2 GPa and Poisson's ratio 0.37. The continuous black lines in Fig. 10 refer to a perfect tangentially loaded Hertzian contact, while the upper grey curves were obtained by decreasing the exponent 1/3 from Eq. (A.2) in steps of 0.01. The bulk stiffness of the pin was estimated according to Eq. (A.1), assuming the same mechanical properties of Polycarbonate mentioned above. Since the pin shortens due to wear after a series of runs, a range of pin heights h between 2 and 3 mm was assumed. Equation (A.1) leads to a range of values between 1.68 MN/m and 2.53 MN/m, indicated in the plots as a horizontal stripe: the bulk stiffness does not depend on normal force. The varying parameter of the GW contact model is σ (see Eq. (A.3)). The black dashed lines shows the result for an initial σ value of 0.4×10^{-5}, and the dashed grey lines were obtained by increasing σ in steps of 0.4×10^{-5}.

All these stiffness estimates fall in the same general range as the measurements, but the detailed pattern is quite complicated. The first cluster of subset 1, with normal force approximately 15 N, shows a good fit with the Hertzian-based stiffness as might be expected with a new, unworn pin. However, once wear occurs none of the later clusters follow the Hertzian trend for increasing normal forces. The reason of the mismatch for the remaining fitted values may lie in the change of real contact area caused by wear. Note that in a previous study [6], different values of the power law exponent in Eq. (A.4) were found for increasing sliding speeds. Because of a lack of estimated $\beta(\omega)$ functions at higher normal forces and sliding speeds, it was not possible to apply the same fitting methodology here. The estimated bulk stiffness has the same order of magnitude as the measured results: it tends to lie slightly higher than the tests for Set 1, but is comparable to many of the later measurements in Set 2 when pin wear was more extreme.

Concerning the GW contact model, the steeper slope of the dashed lines does not seem to match any visible trend of the fitted stiffness values. Indeed, for the fitted values of Set 2 it is hard to discern any systematic trend in the results. Subsets 5–7 show particularly strong scatter. Most of the extreme stiffness values occurred within squeal regions, but there is also a cluster in a non-squealing region near the end of the test sequence (see Fig. 9b). It may be relevant that the pin was extremely worn by this stage. The pattern of the measured clusters of subsets 1–4 may hint at a power law trend lying between the Hertzian and

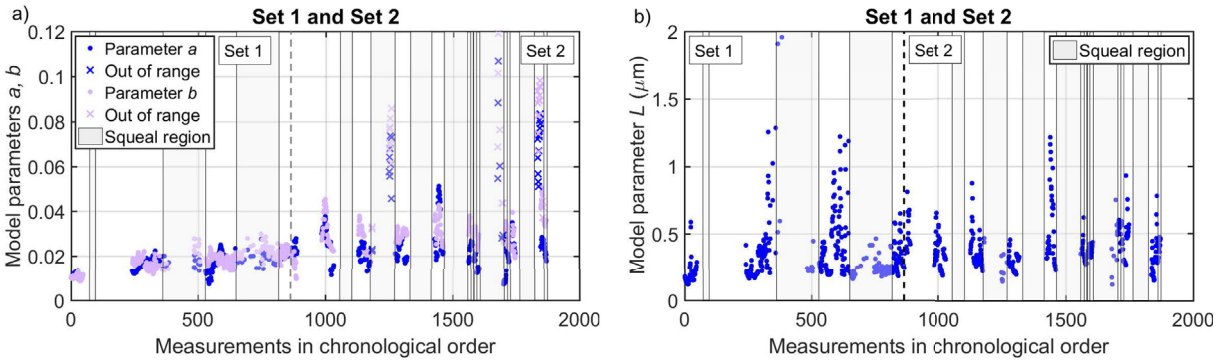

Fig. 11. Variation over time and for different testing conditions of the identified model parameters from experimental data Set 1 and Set 2: (a) model parameters a and b; (b) model parameter L.

Table 1
One-way ANOVA applied on the identified model parameters of data set 1 and data set 2.

F-statistic	Model parameters				
	a	b	$(a-b)$	L	k_t
$F_{cr}(\alpha = 0.05)$	3.8	3.8	3.8	3.8	3.8
F-value	154.2	369.7	167.4	9.8	230.0
p-value	3.6e-32	1.4e-66	1.6e-34	1.9e-03	5.1e-45

GW cases, since both sets of curves seem to catch some combinations of clusters, but the evidence is not compelling.

Next, results are shown for the parameters of the rate-and-state friction model: Fig. 11 shows the variation over time, and for different testing conditions, of the identified model parameters a, b and L. The format is similar to Fig. 9, with squeal regions indicated. The values of a and b identified for Set 2 seem to be somewhat more widely scattered than those for Set 1. As observed for the stiffness k_t, both parameters show an underlying trend to increase over time, but this trend is quite weak compared to the variability. On the other hand, parameter L shows a fluctuating trend over time, with no obvious trend and a pattern that seems to be independent of that of a, b and k_t.

Fig. 11 also highlights that some identified parameters show occasional bursts of rapid increase. For Fig. 11a, most of these jumps are related to the "outliers" observed in Fig. 9b. On the other hand, the occasional rapid and temporary increases of parameter L seem to occur in regions where no squeal event was observed.

It is useful to compare the parameter values reported here with similar model parameters published in the literature. Experimental evidence for a wide variety of material combinations indicates that the parameter $(a-b)$ can range between a maximum of 0.15 [38] and a minimum of −0.2 [39], although most of the observed values lie within a narrower range around $\pm(10^{-3}–10^{-2})$ [33]. Commonly observed values of the length-scale L from laboratory tests are typically on the order of 1 μm [17], but large discrepancies can be found for values estimated by geodetic inversion from real fault motion data, which suggests value of L of the order of $10^{-3}–10^{-2}$ m [40]. Reassuringly, the values obtained from the current study fit well within the most frequent ranges provided in the literature (see Table 2 for more details).

Table 2
Median and MAD values for the identified model parameters of data set 1 and data set 2.

	Statistic	Model parameters				
		a	b	$(a-b)$	L(μm)	k_t(MN/m)
Set 1	mean value	0.017	0.018	−0.001	0.342	1.003
	σ	0.003	0.003	0.003	0.156	0.184
	c_v (%)	18	17	300	54	18
Set 2	mean value	0.025	0.031	−0.007	0.391	1.899
	σ	0.007	0.007	0.008	0.164	1.117
	c_v (%)	28	23	114	42	59

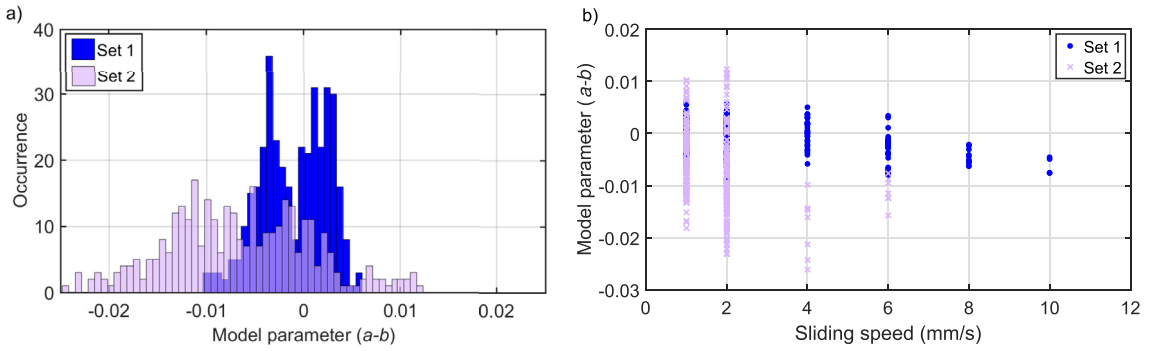

Fig. 12. (a) Distribution of the fitted $(a-b)$ parameter for Set 1 and Set 2; (b) variation of $(a-b)$ plotted against sliding speed.

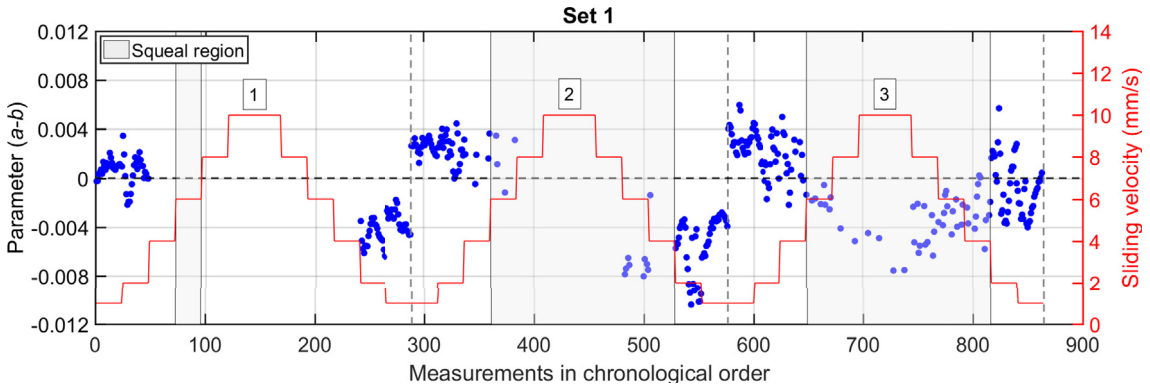

Fig. 13. Variation of the identified $(a-b)$ (blue dots) over time for the dynamic friction measurements of data Set 1. The staircase line and the right y-axis display the sliding velocity of the disc. (For interpretation of the references to colour in this figure legend, the reader is referred to the Web version of this article.)

4. Implications for squeal

4.1. Transitions from velocity weakening to strengthening behaviour

The results just described can be used to shed some light on the occurrences of squeal. The first topic to examine concerns velocity-weakening or velocity-strengthening behaviour of the friction law. If a steady-state condition for the Dieterich-Ruina law (Eq. (6)) is assumed, it can be observed that the amplitude variation of the friction slope f'_{ss} is driven by changes of the sliding velocity and of the normal force (see Eq. (8)). The sign of the parameter $(a-b)$ determines if the friction force has velocity weakening or strengthening behaviour. In the earlier literature, this parameter $(a-b)$ was originally envisaged as a constant, and its sign regarded as an intrinsic property of the contact configuration.

However, the experimental results presented here give a different perspective on $(a-b)$: they show that it varies significantly with time. It turns out that the distribution of the estimated values of $(a-b)$ for Set 1 is slightly different from that of Set 2. Fig. 12a compares the two distributions: the estimates of $(a-b)$ are skewed towards negative values for Set 2, while the estimates for Set 1 are more uniformly distributed between positive and negative values. Furthermore, variations in amplitude and sign of the parameter $(a-b)$ occur within measurements performed at constant sliding speed, as shown in Fig. 12b. Transitions between positive and negative values, and hence between velocity-weakening and velocity-strengthening regimes, are evident for sliding speeds up to 6 mm/s, while for higher speeds a lack of data prevented the identification of a full pattern.

Fig. 13 allows the observed variation to be investigated in more detail. For the sake of clarity, the estimates of $(a-b)$ defined by the bue dots refer to Set 1 only, since subset 3 contains the highest number of successfully estimated $\beta(\omega)$ functions within the squealing region. Two distinctive features can be observed in Fig. 13: a tendency for $(a-b)$ to decrease with increasing sliding speed, and significant variation of this parameter at any given sliding speed. The first feature is clearly observable only for subset 3, while the second one can be detected in all subsets, and also in the results for Set 2 (not shown here). In particular, at sliding speeds of 2 mm/s, 4 mm/s, and in one case also at 6 mm/s, these variations include changes in both amplitude and sign.

Squeal events seem to occur when $(a-b)$ is negative — but not all regions with negative values lead to squeal. The first branch of subset 2 gives an interesting test case. At a sliding speed of 6 mm/s, most of the instantaneous $\beta(\omega)$ functions lead to positive $(a-b)$ values. Note, too, that in Fig. 4a the same first branch appears to show velocity-strengthening behaviour: but

nevertheless a squeal event occurs. This squeal event can be related to one of the identified instantaneous $\beta(\omega)$ functions, which exhibits a negative value of $(a-b)$. In a similar way, the first branch of the $\mu_k - v_0$ curve of subset 3 (see Fig. 4a) seems to exhibit velocity-strengthening behaviour, and yet squeal events at 6, 8 and 10 mm/s occur. However, the friction force-velocity slopes identified through the instantaneous $\beta(\omega)$ function consistently show velocity-weakening behaviour. Experimental details of two of these particular cases are provided in section 4.2.

The observed capricious variations of $(a-b)$ are presumably caused by dynamical processes of some kind taking place at the contact interface, which are quite difficult to measure. Several studies in the literature have pointed out that besides a velocity-weakening regime, there are other candidates that could trigger friction-induced instability phenomena, including variability of transfer layers, wear occurrence and pattern evolution of roughness [41–43], interactions between contact stiffness heterogeneities and different contact pressure distributions [44], thin interface layers that may not behave like the bulk material due to cracks, inhomogeneities and discontinuities [45], and thermal effects [46]. Excluding thermal effects, there is no evidence so far on whether or not the above-mentioned factors could effectively induce changes to the $(a-b)$ term.

Some evidence of variation of $(a-b)$ has been found in the fault mechanics community, and a similar transition behaviour between the two regimes has been experimentally observed [47]. The latter study showed that changes of the parameter $(a-b)$ were related to both measured temperature and normal stress variations for the tested material combination during sliding friction experiments. A similar correlation has been investigated theoretically through a microphysical rate-and-state model [48], where the sign and amplitude $(a-b)$ depends on the ratio between the contact shear and normal stress and contact surface temperature, respectively. A more elaborate model, the "CNS" model [35], makes an attempt to simulate the deformation of a granular fault gouge contact interface by taking into account the granular flow in combination with thermally activated creep and intergranular sliding. In this case, the parameter $(a-b)$ turns out to be nonlinearly dependent on sliding velocity, temperature and fault depth. A more recent study [36] tackles the derivation of microphysical rate-and-state models by assuming that sliding is followed by a thermally activated visco-plastic deformation of junctions in their entire volume, not limited to a thin layer at asperity level. Under steady-state conditions, the friction coefficient was explicitly related to sliding velocity, temperature, microscopic normal stress acting on the plastic junctions, geometrical contact parameters and rheological properties of the material in contact. The results showed that the transition from velocity strengthening to weakening can happen for an increase in temperature and decrease in sliding velocity. Critical temperatures have been also defined marking the transitions from a stable to an unstable regime and vice versa.

In the context of the present measurements of variation of $(a-b)$, it seems plausible to speculate that temperature and small variations of normal stress caused by the non-flatness of the disk and the induced excitation may have played an important role. Additionally, as temperature increases, the viscoelastic behaviour of a polymer like Polycarbonate goes from the glassy region to the glass transition region. If temperature is further increased a rubbery plateau domain is reached, which eventually leads to viscous flow behaviour. For a material like Polycarbonate this full transition can occur over a temperature range between 120 and 240 °C [49].

4.2. Squeal prediction and examples

To the best of the authors' knowledge, rate-and-state models have not previously been used to capture friction-induced instabilities such as squeal phenomena at mid-high frequency. These models have been used extensively within the geomechanics community, but there they are usually applied to sliding friction tests carried out at far lower sliding speeds than the ones used here. This section gives a first glimpse of the use of rate-and-state models for squeal prediction, to explore the potential benefits of using estimates of $\beta(\omega)$. The model to be used here is the simplest possible: note that a detailed discussion of the pitfalls of over-simplified models for quantitative squeal prediction has appeared in earlier literature [7,8].

In a back-of-the-envelope fashion, Appendix B briefly illustrates squeal prediction based on a rate-and-state law. If only one degree of freedom is considered, it is shown that a Hopf bifurcation leading to instability is possible if $(a-b)$ is negative. The critical frequency ω_c^2, given in Eq. (B.4), depends on the rate-and-state friction parameters and the sliding speed, so it can be estimated and tracked using the identified model parameters and their variation over time. The blue crosses in Figs. 14 and 15 show the estimates of ω_c^2. The observed squeal events for both data sets were confined to the regions marked by grey bands. The red lines indicate the sliding speed, increasing then decreasing for each subset, corresponding to the first and second branches of the $\mu_k - v_0$ curves shown in section 3.2. The proportional relation between ω_c^2 and v_0 is clearly visible in Set 1, subset 3.

To add some detail to the results summarised in Figs. 14 and 15, and to visualize the data processing procedure, two illustrative examples are now shown. The first example, in Fig. 16, refers to subset 3 of Set 1, measured at a sliding speed of 8 mm/s during a test sequence of increasing speed. As pointed out in subsection 4.1, this squeal event occurs within the first branch of the $\mu_k - v_0$ curve shown in Fig. 4a, which apparently exhibits velocity-strengthening behaviour. To visualize the squeal occurrence, a time-frequency analysis was performed on the time series recording the acceleration along the sliding direction. The resulting spectrogram shows pronounced intermittent squealing around 2.1 kHz. This frequency corresponds to the first tangential mode of the dynamometer [6,50]. Two further peaks at lower amplitude can also be detected near 1.4 kHz and 1.6 kHz, which usually show up in both the tangential and normal motion and are again linked to test-rig resonances.

It only proved possible to obtain good model fits for two $\beta(\omega)$ functions measured during this run, from the 5 s segments indicated by the numbers 1 and 2. The first occurs at the onset of a squeal event and the second during a squeal event. The Nyquist plots of both $\beta(\omega)$ functions are plotted in Fig. 16b–c, covering a frequency range between 0.1 and 3 kHz. Both functions cross into the right half-plane at a critical frequency ω_c. This marks the onset of velocity-weakening behaviour of the frictional

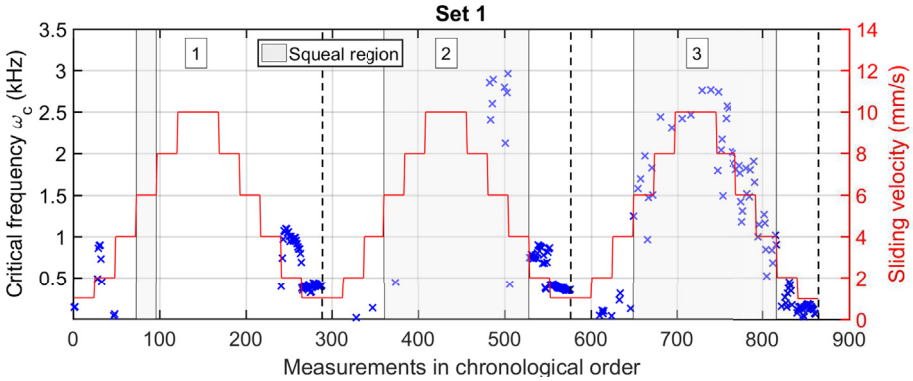

Fig. 14. Estimation and variation of the critical frequency ω_c (blue crosses) against time for the dynamic friction measurements of data Set 1. The right y-axis displays the sliding velocity of the disc. (For interpretation of the references to colour in this figure legend, the reader is referred to the Web version of this article.)

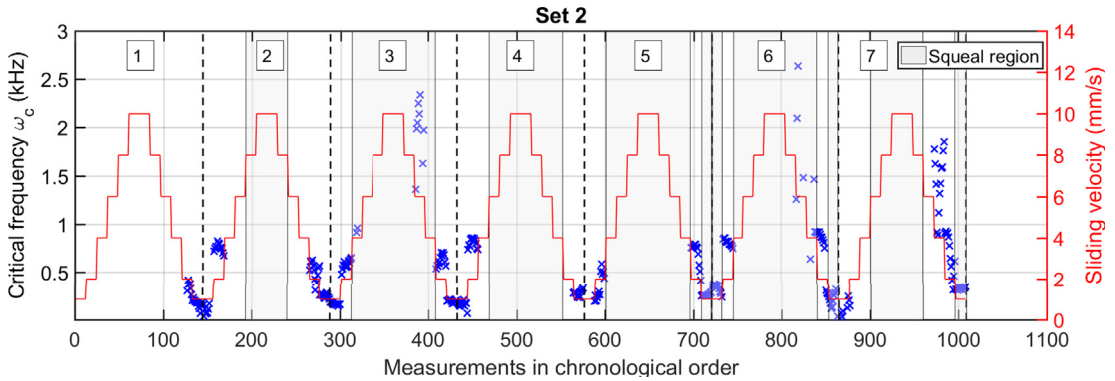

Fig. 15. Estimation and variation of the critical frequency ω_c (blue crosses) against time for the dynamic friction measurements of data Set 2. The right y-axis displays the sliding velocity of the disc. (For interpretation of the references to colour in this figure legend, the reader is referred to the Web version of this article.)

interface, in clear contrast to what was suggested by the $\mu_k - v_0$ curve. Each Nyquist plot contains the information for the fitted model parameters, operational conditions and the estimated ω_c. The critical frequency is 2.44 kHz for case 1 and 2.31 kHz for case 2, both above the observed squealing frequencies and thus correctly indicating unstable behaviour. It should be noted that the resonance peak near 2.1 kHz, and also the two lower ones around 1.5 kHz, are usually visible in the raw measurements of $\beta(\omega)$. However, in order to allow a clear representation of the underlying functional form of $\beta(\omega)$, these rig artefacts have been filtered out without significantly changing the shape of $\beta(\omega)$, as described in an earlier publication [1].

This example is typical of most of the squeal cases occurring at speeds higher than 6 mm/s, for which the most pronounced squealing frequency is always near 2.1 kHz. This fits neatly with what Figs. 14 and 15 reveal: the ω_c estimates only rise above this frequency for sliding speeds of 6 mm/s and above.

Fig. 17 shows the second squeal example, which refers to Set 1, subset 2 measured at a sliding speed of 6 mm/s during a test sequence of increasing speed. The squealing pattern is less pronounced, but fairly similar to the one just discussed. However, this example is instructive because the only four segments leading to satisfactory model fits to $\beta(\omega)$ fall in time intervals where the system was *not* squealing. Three of the four show a Nyquist plot confined to the left half-plane. The remaining $\beta(\omega)$ function (case 3) does show a Nyquist circle crossing to the right half-plane, but only at a frequency $\omega_c = 0.44$ kHz, insufficient to cause instability at 2.1 kHz. It is interesting to note the rotation of $\beta(\omega)$ towards the right half-plane when approaching two pronounced squeal events (cases 2 and 3).

5. ANOVA and exploratory factor analysis

In sections 3.3 and 4.1 the variation of each of the identified rate-and-state parameters a, b, L and $(a-b)$ and the stiffness parameter k_t was investigated independently. By linking the results with what has been found in the literature, it was suggested that unobserved and/or uncontrolled factors such as temperature and wear are probably driving the observed variability. In order to probe this preliminary conclusion further, a more quantitative analysis was carried out. The two data sets were tested in order to quantify the statistical similarity or dissimilarity by means of an analysis of variance (ANOVA) [51]. Subsequently, a

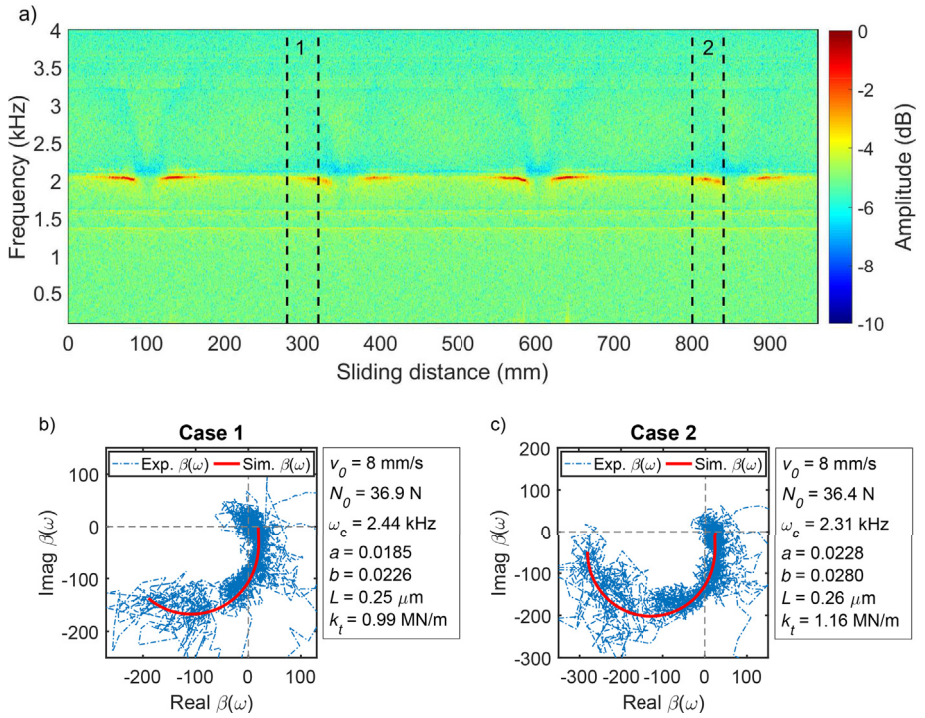

Fig. 16. (a) Spectrogram of the measured tangential velocity v'. The black dashed lines indicate the 5 s time-segment for which $\beta(\omega)$ was estimated; (b)–(c) Nyquist plots of $\beta(\omega)$ where the blue lines refer to the experimental data, while the simulated data corresponds to the red line. The model parameters are listed on the right side. (For interpretation of the references to colour in this figure legend, the reader is referred to the Web version of this article.)

correlation and factor analysis [51] was applied in an effort to establish the number of independent factors driving the process.

The ANOVA test aims at quantifying the statistical difference or similarity between Set 1 and Set 2. A one-way ANOVA analysis was carried out independently for each model parameter, to test for statistically significant differences in the means between the two data sets. The test is based on computing the *F*-value, which is the ratio of two variances: the variance between sample means estimated for each data set and the variance within the samples for each data set. These two quantities are expected to be approximately similar if the null hypothesis is true. In order to check the validity of the null hypothesis, the *F*-value is placed within the Fisher distribution and the *p*-value probability is then calculated. The *p*-value estimates the likelihood of a sample occurring due to chance, given the assumed sampling distribution. If this probability is lower than a chosen threshold α, the null hypothesis can be rejected. The α level chosen here was 5%; it defines the probability of mistakenly rejecting the null hypothesis. An alternative and consistent way to assess the statistical similarity between the data sets is to compare the computed *F*-value with a critical value F_{cr} value, inferred from a Fisher distribution for a given value of α. For the null hypothesis to be true, *F* must be lower than F_{cr}.

Table 1 displays the values of *F* and *p* for each model parameter. The *F*-values are all higher than the computed F_{cr}. Similarly, all the estimated *p*-values are lower than the threshold defined by α. It can be concluded that the dissimilarity between the model parameters identified from Set 1 and from Set 2 is statistically significant. Given the dissimilarity, the mean values, the standard deviation (σ) and the corresponding coefficient of variation c_v of each model parameter have been computed for each data set separately and listed in Table 2. The coefficients of variation highlight an increase of scatter in Set 2 for model parameters *a*, *b* and k_b. On the other hand, the values of parameter $(a-b)$ and *L* are more spread in Set 1 than in Set 2. This can be explained by the fact that Set 1 exhibits a symmetric distribution of $(a-b)$ around the transition point, while the distribution of $(a-b)$ in Set 2 tends to be skewed towards negative values (see subsection 4.1 and Fig. 12a).

Despite this quantified dissimilarity, a factor analysis based on the complete combined data set was also carried out. The aim was to identify the minimum number of common latent factors able to explain the observed model parameter variation, and the degree of correlation among such parameters. Since factor analysis implicitly assumes a linear correlation between observed variables and latent factors, a first qualitative screen on the existing correlation was performed.

Fig. 18 qualitatively indicates some possible correlation patterns among the identified model parameters. In both figures the values for Set 1 and Set 2 are distinguished by colour. Independently of this separation, Fig. 18a indicates that an increase in tangential stiffness leads to an almost linear increase of both parameters *a* and *b*. Since the change of the tangential stiffness is most likely caused by wear, it seems plausible to assume that parameters *a* and *b* are also driven by the same factor. Note that such linear correlation is more neat for Set 1, while the parameters for Set 2 exhibit more scatter.

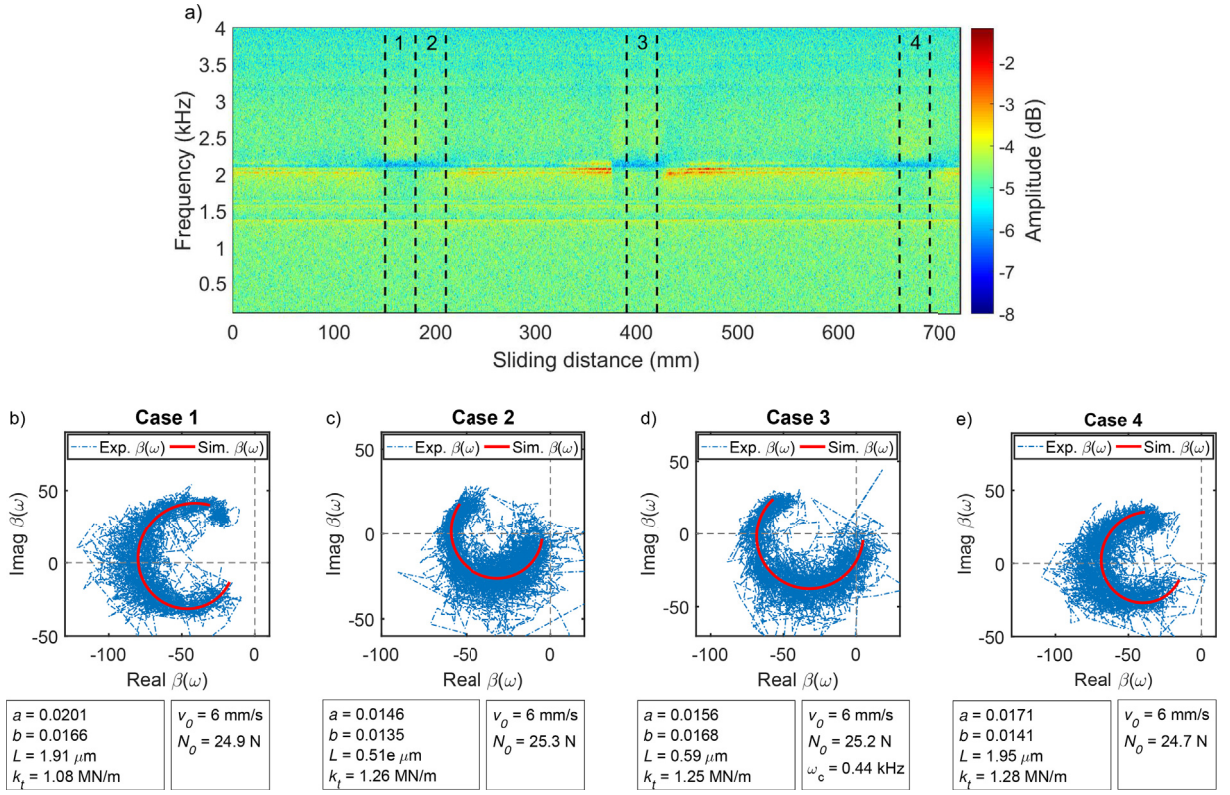

Fig. 17. (a) Spectrogram of the measured tangential velocity v'. The black dashed lines indicate the 5 s time-segment for which $\beta(\omega)$ was estimated; (b)–(e) Nyquist plots of $\beta(\omega)$ where the blue lines refer to the experimental data, while the simulated data corresponds to the red line. The model parameters are listed on the right side. (For interpretation of the references to colour in this figure legend, the reader is referred to the Web version of this article.)

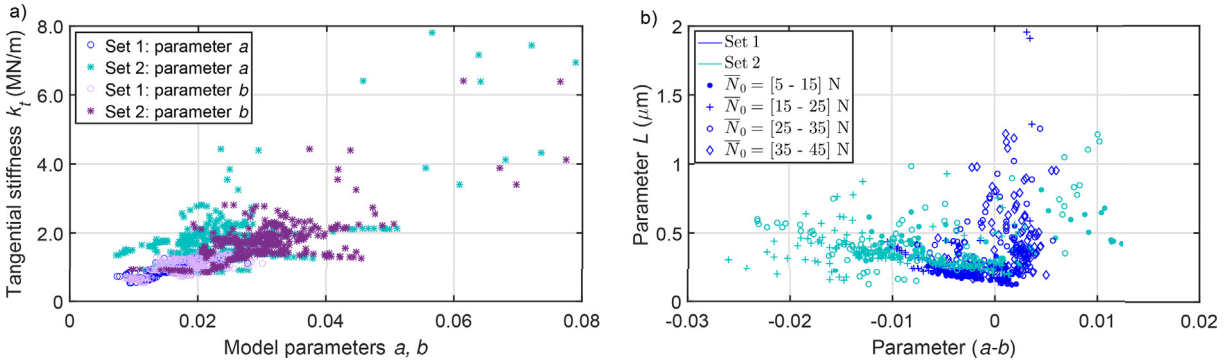

Fig. 18. (a) Variation of parameters a, b and k_b for all data set; (b) Parameters $(a-b)$ vs. parameter L for all data set. For Fig. 18b, the data was divided in four clusters based on normal force ranges as indicated in the legend.

The relation between the length-scale parameter L and the parameter $(a-b)$, which defines the sign of f'_{ss}, is more peculiar. Experimental evidence in the geomechanics community usually suggests values of L which are independent of operational conditions [17,21], and it is often treated as a "universal constant". This viewpoint has been already challenged conceptually [19,20], experimentally [6] and in terms of models [52,53]. In particular, the latter two studies investigated the collective behaviour of an ensemble of viscoelastic elements representing contact asperities sliding on a rough surface. The simulated collective response suggested a sliding velocity dependence of the characteristic length-scale L. This velocity dependence was also observed experimentally [1,6] for specific material combinations.

This study adds a further twist to the story. A linear correlation between parameter L and the parameter $(a-b)$ can be observed in Fig. 18b within a velocity weakening regime. However, there is a qualitative change of behaviour when $(a-b)$ changes sign, the transition point between velocity-weakening and velocity-strengthening regimes. To the best of the authors'

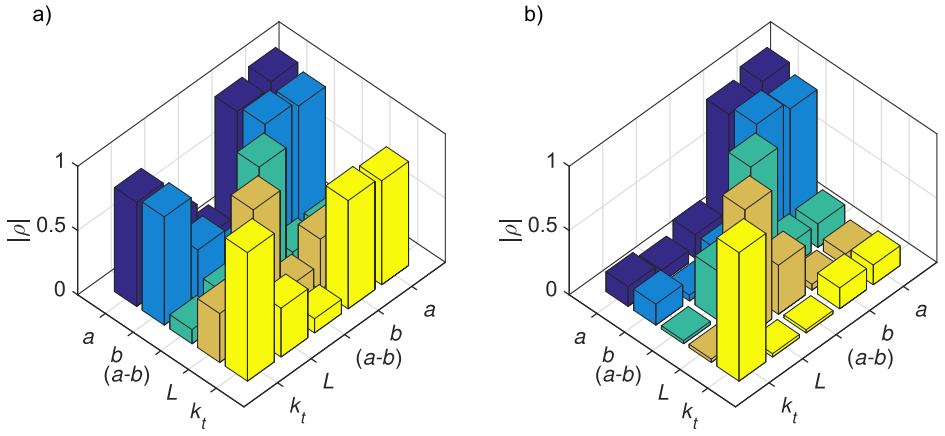

Fig. 19. Matrix of Pearson's correlation coefficients for: (a) velocity-strengthening regime; (b) velocity-weakening regime.

Table 3
Summary of factor analysis results: number of factors, factor loadings and eigenvalues of the decomposed correlation matrix.

Parameters	Estimated factor loadings: $r_{ij} = \sqrt{\lambda_i} e_{ij}$			
	Velocity-strengthening		Velocity-weakening	
	I_1	I_2	I_1	I_2
a	0.96	0.08	0.97	−0.15
b	0.96	−0.20	0.97	0.16
$(a-b)$	0.01	0.93	0.01	−0.85
L	0.58	0.46	−0.04	0.81
k_t	0.90	−0.18	0.31	0.10
Eigenvalues	2.99	1.67	1.98	1.43

knowledge, such behaviour has not previously been reported in the literature of rate-and-state models. It is worth noting that the lowest values of L tend to occur at the transition point when $(a-b)$ approaches zero, while the velocity-strengthening regime seems to exhibit more spread and higher values of the length-scale parameter. The latter observation seems to support the hypothesis that higher values of L means greater frictional strength [54]. In fact, the characteristic length-scale L is often regarded as a measure of asperity contact maturity, indicating the slip distance necessary to regain a steady frictional strength after a perturbation in the loading conditions has been applied. It is worth comparing the observed behaviour of parameter L in Figs. 11b, 17 and 18b. The main conclusion seems to be that decreasing behaviour of L may indicate that the interface mechanics is approaching a state which may be prone to instability.

Given this distinctive behaviour between the velocity strengthening and weakening regimes, the combined data set (Set 1 + Set 2) has been split according to these two regimes, and a factor analysis was applied separately on both sets. The general linear regression model upon which factor analysis relies is given by

$$\mathbf{X} = \mathbf{RI} + \boldsymbol{\epsilon} \tag{11}$$

where the vector $\mathbf{X}$ contains the measured (or identified) dependent variables, $\mathbf{R}$ is the matrix of factor loadings representing the regression coefficients, $\mathbf{I}$ is the vector of latent factors or independent variable, and $\boldsymbol{\epsilon}$ defines additional sources of variation, also called specific factors. The general aim is to estimate the factor loading, the number of factors and the specific factor. In the following study, attention is focused only on the number of factors that drive the observed parameter variation, to which end a first-stage exploratory factor analysis has been performed. In order to extract the necessary information from measured data, certain assumptions on the covariance relationships are required: see Ref. [51] for further details. The factor estimation technique then employs a principal component analysis of the correlation matrix estimated for each data set. Fig. 19 shows the absolute values of the Pearson linear correlation coefficient ρ between each pair of identified model parameters, and Table 3 summarizes the results of the factor analysis in terms of identified number of factors and factor loadings. For clarity, r_{ij} defines the estimated regression coefficients referred to the factor i and parameter j, λ_i is the selected eigenvalue and e_{ij} is the corresponding eigenvector obtained from the principal component analysis.

For both regimes, it appears that two main factors are needed to account for the variation of the identified model parameters. The number of main factors was selected based on the "eigenvalue greater than one" rule [51], since a principal component anal-

Table 4
Propagation of rate-and-state model variability to the estimates of ω_c.

Parameters	Set 1: $\omega_{c,ref} = 225$ (Hz)		Set 2: $\omega_{c,ref} = 339$ (Hz)	
	$\lvert\Delta\omega_c\rvert$ (Hz)	c_v (%)	$\lvert\Delta\omega_c\rvert$ (Hz)	c_v (%)
$\Delta(a-b)$	225	100	231	68
ΔL	189	84	288	85

ysis of the correlation matrix of standardized data was performed. The eigenvalues quantify how much variance of the observed variables can be explained by each specific factor. A factor with $\lambda_i > 1$ explains more variance than any single parameter.

A more detailed analysis based on the Pearson correlation coefficients, shown in Fig. 19, and the estimated factor loadings, shown in Table 3, reveals different patterns for the two regimes. During the velocity-strengthening regime, three parameters (a, b and k_t) show a high correlation with the first identified factor and also with each other. The second identified factor tends to explain the observed variation of $(a-b)$. On the other hand, note that in order to explain the variation of parameter L, both factors are needed. This correlation pattern changes during a velocity-weakening regime. The first factor is able to explain only the variation of parameters a and b, while the identified stiffness k_t exhibit a low correlation with respect to I_1 and an almost negligible linear relation with I_2. The second factor seems to drive the variation process of parameter L and $(a-b)$. Their correlation was already highlighted in Fig. 18b.

Since the variability of the identified rate-and-state model parameters has been quantified, it is worth assessing how this variability propagates into squeal prediction by exploiting Eq. (B.4). According to Table 2, the lowest coefficient of variation is 17%, while the largest one reaches 300%. Since the estimation of the critical frequency ω_c relies on these model parameters, it is hardly surprising that robust squeal prediction is often an elusive task [8,10,13]. Table 4 quantifies the effect of the estimated model parameter variations on the critical frequency. The reference critical frequency, $\omega_{c,ref}$, was computed based on the estimated mean values for both data sets. The standard deviations for each identified model parameter were then used to compute the variation of the critical frequency, $\Delta\omega_c$. Deviations of 100% from $\omega_{c,ref}$ can be observed, while the smallest variation is about 68%. This last observation underlines the importance of linking rate-and-state model parameters to physical properties of the materials in contact, in order to predict in advance eventual model parameter variability caused by operational factors.

6. Conclusions

This paper has examined in some detail the dynamic friction behaviour of a Polycarbonate pin sliding against a steel disc, a case for which it had previously been found that the test rig for measuring and estimating the frictional frequency response function $\beta(\omega)$ was prone to intermittent friction-excited squeal. The procedure described previously for estimating $\beta(\omega)$ was modified to allow "instantaneous" estimates. Data segments of length 5 s were used, and in many cases it proved possible to obtain a satisfactory fit of a rate-and-state friction model including the effect of tangential contact stiffness: the same type of model previously shown to work well for a variety of material combinations [1]. The "instantaneous" estimates of $\beta(\omega)$ were able to capture the dynamic friction behaviour at the onset of squeal, after squeal and in a few cases even during a squeal event.

As a result of these new measurements, the variation in time of the model parameters could be tracked and the pattern compared with the observed occurrences of squeal. Variations in time were of two types. First, some model parameters exhibited systematic trends, probably associated with wear of the pin and with rising temperature during the testing sequence. The contact stiffness k_t showed an increasing trend with time as successive test cases were run using the same pin. The rate-and-state friction model involves two non-dimensional parameters a and b, and a length-scale parameter L (see Eq. (8)). Of these, a and b showed increasing trends similar to that of k_t, while the behaviour of L was more complicated.

The second type of variation observed in the results was apparently random, perhaps associated with unmeasured details of the transferred film of wear debris on the surface of the disc and/or to unobserved dynamic processes that may take place at the interface. These random variations seem to be responsible for the intermittent nature of squeal events in the test rig. A key conclusion of this work is that the dynamic frictional frequency response $\beta(\omega)$ may indicate "velocity-weakening" frictional behaviour for a range of frequencies, even though the apparent slope of the "Stribeck curve" deduced from steady-sliding tests indicates velocity-strengthening behaviour. Transitions between velocity-weakening and velocity-strengthening behaviour of $\beta(\omega)$ can be tracked by inspecting the sign of a single variable in the friction model: the combination $(a-b)$.

The capability of the proposed methodology to track and distinguish the two different dynamic friction regimes is of great importance when it comes to predicting the occurrence of squeal instability. When $(a-b) < 0$, the Nyquist plot of $\beta(\omega)$ crosses into the unstable right-hand half of the complex plane. Within the simplest model for friction-excited vibration, with a single degree of freedom oscillator, a Hopf bifurcation occurs at the frequency where this crossing happens. If the natural frequency of the oscillator lies below the critical frequency ω_c of the bifurcation, unstable growing oscillation is predicted. Examples of squeal occurrences have been shown, where the behaviour of $\beta(\omega)$ seems to lend support to this simple picture. This success makes it immediately plausible that the capability of the instantaneous $\beta(\omega)$ function to track short-time transitions could be an important new tool for understanding squeal.

A preliminary attempt has been presented to use Factor Analysis to probe possible connections between variation of the different parameters. It appears likely that most of the variability can be attributed to the influence of two controlling factors, but that the details of these two factors are different for the cases of velocity-weakening and velocity-strengthening friction, as

indicated by the sign of the variable $(a - b)$. This is strikingly illustrated by the different correlation patterns observed between parameter $(a - b)$ and L for the two different friction regimes. This result surely deserves further investigation.

In the authors' opinion, the new methodology of tracking dynamic friction in a time-dependent manner opens up many possible new research directions. It would be straightforward in principle to apply the approach to materials of more obvious technological significance that Polycarbonate; for example brake-liner compounds. At a more fundamental level, the testing methodology could be further enhanced to enable the identification of a $\beta(\omega)$-like function associated with deformation in the direction normal to the contact surfaces: the same theoretical work motivating the original measurement of $\beta(\omega)$ suggested that this might be important [7]. Concurrently, as suggested by the results presented here, parameters such as surface temperature should be added to the list of factors to measure.

It can be hoped that incorporating factors like temperature, wear and normal force fluctuation into the modelling would provide at least a partial explanation for some of the observed systematic trends and apparently random variation. Understanding such "capricious" aspects of frictional behaviour has been an elusive goal of research for many years, and this new experimental tool has the potential to spark important progress. In a different avenue of theoretical development, the proposed concept of measuring $\beta(\omega)$ could be extended to larger conformal contact interfaces, to replicate the contact scenario of real applications and to explore whether new mechanisms for instability are then predicted. The more the testing methodology could be improved, the more likely it is that further physical hints would emerge to explain the parameter variation and to validate microphysical-based friction models.

CRediT authorship contribution statement

A. Cabboi: Conceptualization, Methodology, Validation, Formal analysis, Data curation, Investigation, Writing - original draft, Visualization. **J. Woodhouse:** Conceptualization, Supervision, Writing - review & editing.

Declaration of competing interest

The authors have no conflicts of interest to declare.

Acknowledgements

The authors would like to thank Dr. Thibaut Putelat for stimulating discussions on rate-and-state models, typically applied in the geomechanics community, Dr. Tore Butlin for helping in organizing the experimental campaign performed in September 2018, and Dr. Alice Cicirello for providing feedback on the manuscript. The authors both acknowledge the initial support from the EPSRC programme Grant "Engineering Nonlinearity" (ref. EP/K003836/1).

Appendix A. Estimation of contact stiffness

To check the magnitude of the tangential stiffness extracted from the measured $\beta(\omega)$ functions it is useful to compare with simple estimates to be found in the literature. One can envisage three contributions: the pin's bulk shear stiffness, the interfacial Hertz-Mindlin contact stiffness, and the interfacial stiffness derived from asperity contacts on rough surfaces.

A simple guess of the pin's bulk stiffness can be obtained by assuming the pin to be a thick cylindrical cantilever rod subject to shear deformation. The elastic compliance is then given by Ref. [55].

$$k_b = \frac{GAc}{h} \quad \text{where} \quad c = \frac{6(1+\nu)}{7+6\nu} \quad \text{for circular cross section} \tag{A.1}$$

where A is the area of the cylinder, c is the Timoshenko shear coefficient, h is the height of the pin and G is the shear modulus.

According to Mindlin [56] the contact compliance of a tangentially and normally loaded elastic hemisphere pressed against a rigid half-space can be expressed as

$$k_i = \left(\frac{4E}{(1+\nu)(2-\nu)}\right)\left(\frac{3R(1-\nu)N_0}{4E}\right)^{1/3} \tag{A.2}$$

where R is the radius of the hemisphere, N_0 is the normal load, E is the Young's modulus and ν is Poisson's ratio.

Finally, for a conformal contact satisfying the Greenwood-Williamson assumptions [57,58], the contact compliance of a tangentially loaded rough surface pushed against a rigid half-space with no slip can be written

$$k_i = 2\frac{(1-\nu)}{(2-\nu)\sigma}N_0 \tag{A.3}$$

where σ is the standard deviation of the asperity heights.

Note that all these contributions to tangential contact stiffness depend on the normal force N_0 through a power law [59] with the general form

$$k_i = \kappa N_0^{\alpha} \tag{A.4}$$

The parameters κ and α are not known a priori, but each of the special cases just noted gives a particular value of the exponent α. For the bulk stiffness, the value is zero (i.e. no dependence on N_0); for the Hertzian case the exponent is 1/3; and for the Greenwood-Williamson case a linear proportionality is obtained, corresponding to $\alpha = 1$.

Appendix B. Critical frequency ω_{cr} for a SDOF system

The frequency response of dynamic friction is the required friction information which naturally enters in any linearised stability analysis. The simplest example of such a stability analysis is presented in this appendix: the critical frequency at the onset of instability for a single mass m, attached to a fixed base through a spring k and sliding on a belt driven at speed v_0. At the sliding interface, a frictional force F is generated which is assumed to follow the rate-and-rate law. The characteristic equation of this system is obtained by retaining only the first order terms from a Taylor expansion of the perturbed equation of motion, and reads as follows

$$\frac{1}{m}\frac{1}{(\omega_0^2-\omega^2)} = \frac{1}{i\omega\beta_{CP}(\omega)} \tag{B.1}$$

where $\omega_0^2 = k/m$ is the natural frequency of the system.

The onset of instability of the system in Eq. (B.1) occurs when one of the system poles crosses to the lower Fourier half-plane. Taking into account the expression for the measured frictional response function (see Eq. (9)), the characteristic equation can be rewritten as

$$m(\omega_0^2-\omega^2) = -\omega\Im(\beta_{CP}(\omega)) + i\omega\Re(\beta_{CP}(\omega)). \tag{B.2}$$

The applied perturbation will lead to an oscillatory decay or growth, depending on the sign of the imaginary part of Eq. (B.2). The onset of instability is thus found by setting the imaginary part to zero:

$$i\omega\Re(\beta_{CP}(\omega)) = 0 \tag{B.3}$$

which leads, after some mathematical manipulation, to a Hopf bifurcation [54,60,61] occurring at the critical frequency

$$\omega_c^2 = -\frac{g_{,\phi}^2 f'_{ss}}{f_{,v}} \tag{B.4}$$

For the given friction law and the undamped SDOF system, the critical "Hopf" frequency ω_c^2 occurs only if f'_{ss} is negative. Note that ω_c^2 merely depends on the frictional properties of the contact interface. It defines the frequency at which the measured $\beta(\omega)$ crosses into the right-hand half of the complex plane, as shown in Fig. 3b. An instability may then occur whenever the resonance of the system lies below ω_c.

References

[1] A. Cabboi, J. Woodhouse, Validation of a constitutive law for friction-induced vibration under different wear conditions, Wear 396397 (2018) 107–125.
[2] R. Stribeck, Die wesentlichen Eigenschaften der Gleit- und Rollenlager, Z. Ver. Dtsch. Ingenieure 46 (1902) (38,39) 134248,14337.
[3] S.A. McKee, T.R. McKee, Friction of journal bearings as influenced by clearance and length, Trans. ASME 57 (1929) 161–171 15.
[4] P.J. Blau, Friction Science and Technology: from Concepts to Applications, CRC Press, Taylor and Francis, Boca Raton, USA, 2009.
[5] S. Wang, J. Woodhouse, The frequency response of dynamic friction: a new view of sliding interfaces, J. Mech. Phys. Solid. 59 (5) (2011) 1020–1036.
[6] A. Cabboi, T. Putelat, J. Woodhouse, The frequency response of dynamic friction: enhanced rate-and-state models, J. Mech. Phys. Solid. 92 (2016) 210–236.
[7] T. Butlin, J. Woodhouse, Friction-induced vibration: should low-order models be believed? J. Sound Vib. 328 (1) (2009) 92–108.
[8] T. Butlin, J. Woodhouse, Friction-induced vibration: model development and comparison with large-scale experimental tests, J. Sound Vib. 332 (21) (2013) 5302–5321.
[9] R. Fosberry, Z. Holubecki, Disc Brake Squeal: its Mechanism and Suppression, Tech. rep., Motor Industry Research Association, 1961.
[10] R.A. Ibrahim, Friction-induced vibration, chatter, squeal, and chaos. Part II: dynamics and modeling, Appl. Mech. Rev. 47 (7) (1994) 227–253.
[11] G. Sheng, Friction-induced Vibrations and Sound: Principles and Applications, CRC Press, Taylor and Francis, Boca Raton, USA, 2008.
[12] G. Chen, Z. Zhou, P. Kapsa, L. Vincent, Experimental investigation into squeal under reciprocating sliding, Tribol. Int. 36 (12) (2003) 961–971.
[13] P. Duffour, J. Woodhouse, Instability of systems with a frictional point contact-part 3: experimental tests, J. Sound Vib. 304 (1) (2007) 186–200.
[14] K.G. McConnel, P.S. Varoto, Vibration Testing: Theory and Practice, second ed., Wiley, Hoboken, USA, 2008.
[15] Y. Bar-Sinai, R. Spatschek, E.A. Brener, E. Bouchbinder, Velocity-strengthening friction significantly affects interfacial dynamics, strength and dissipation, Sci. Rep. 5 (2015) (7841).
[16] A.M. Budkov, G.G. Kocharyan, Experimental study of different modes of block sliding along interface. part 3. numerical modeling, Phys. Mesomech. 20 (2) (2017) 203–208.
[17] J.H. Dieterich, Modeling rock friction: 1. experimental results and constitutive equations, J. Geophys. Res. 84 (1979) 2161–2168.
[18] A.L. Ruina, Slip instability and state variable friction laws, J. Geophys. Res. 88 (1983) 10359–10370.
[19] T. Putelat, J.H.P. Dawes, Steady and transient sliding under rate-and-state friction, J. Mech. Phys. Solid. 78 (2015) 70–93.
[20] T. Putelat, J.H.P. Dawes, J.R. Willis, On the microphysical foundations of rate-and-state friction, J. Mech. Phys. Solid. 59 (5) (2011) 1062–1075.
[21] C. Marone, Laboratory-derived friction laws and their application to seismic faulting, Annu. Rev. Earth Planet Sci. 26 (1) (1998) 643–696.
[22] P. Berthoud, T. Baumberger, Shear stiffness of a solidsolid multicontact interface, Philos. Trans. Roy. Soc. A 454 (1998) 1615–1634 1974.
[23] N. Lapusta, J.R. Rice, Nucleation and early seismic propagation of small and large events in a crustal earthquake model, J. Geophys. Res. Solid Earth 108 (B4) (2003) 1–18.
[24] F.M. Chester, Effects of temperature on friction: constitutive equations and experiments with quartz gouge, J. Geophys. Res. Solid Earth 99 (B4) (1994) 7247–7261.
[25] J.R. Rice, Heating and weakening of faults during earthquake slip, J. Geophys. Res. Solid Earth 111 (B5) (2006).
[26] S.A.M. den Hartog, A.R. Niemeijer, C.J. Spiers, New constraints on megathrust slip stability under subduction zone P-T conditions, Earth Planet Sci. Lett. 353354 (2012) 240–252.

[27] E.K. Mitchell, Y. Fialko, K.M. Brown, Velocity-weakening behavior of westerly granite at temperature up to 600°C, J. Geophys. Res. Solid Earth 121 (9) (2016) 6932–6946.
[28] V. Rubino, A.J. Rosakis, N. Lapusta, Understanding dynamic friction through spontaneously evolving laboratory earthquakes, Nat. Commun. 8 (2017) 15991.
[29] M.F. Linker, J.H. Dieterich, Effects of variable normal stress on rock friction: observations and constitutive equations, J. Geophys. Res. Solid Earth 97 (B4) (1992) 4923–4940.
[30] E.R. Heimisson, P. Segall, Constitutive law for earthquake production based on rate-and-state friction: Dieterich 1994 revisited, J. Geophys. Res. Solid Earth 123 (5) (2018) 4141–4156.
[31] V. Popov, B. Grzemba, J. Starcevic, M. Popov, Rate and state dependent friction laws and the prediction of earthquakes: what can we learn from laboratory models? Tectonophysics 532535 (2012) 291–300.
[32] T. Baumberger, P. Berthoud, C. Caroli, Physical analysis of the state- and rate-dependent friction law. ii. dynamic friction, Phys. Rev. B 60 (1999) 3928–3939.
[33] M.J. Ikari, B.M. Carpenter, C. Marone, A microphysical interpretation of rate- and state-dependent friction for fault gouge, Geochem. Geophys. Geosy. 17 (5) (2016) 1660–1677.
[34] K. Tian, D.L. Goldsby, R.W. Carpick, Rate and state friction relation for nanoscale contacts: thermally activated Prandtl-Tomlinson model with chemical aging, Phys. Rev. Lett. 120 (18) (2018) 186101(6).
[35] M. van den Ende, J. Chen, J.P. Ampuero, A.R. Niemeijer, A comparison between rate-and-state friction and microphysical models, based on numerical simulations of fault slip, Tectonophysics 733 (2018) 273–295.
[36] A. Molinari, H. Perfettini, Fundamental aspects of a new micromechanical model of rate and state friction, J. Mech. Phys. Solid. 124 (2019) 63–82.
[37] X. Mao, V.L. Popov, J. Starcevic, M. Popov, Reduction of friction by normal oscillations. II. In-plane system dynamics, Friction 5 (2) (2017) 194–206.
[38] M.L. Blanpied, C.J. Marone, D.A. Lockner, J.D. Byerlee, D.P. King, Quantitative measure of the variation in fault rheology due to fluid-rock interactions, J. Geophys. Res. Solid Earth 103 (B5) (1998) 9691–9712.
[39] L. Buijze, A.R. Niemeijer, R. Han, T. Shimamoto, C.J. Spiers, Friction properties and deformation mechanisms of halite(-mica) gouges from low to high sliding velocities, Earth Planet Sci. Lett. 458 (2017) 107–119.
[40] M. Kano, S. Miyazaki, Y. Ishikawa, Y. Hiyoshi, K. Ito, K. Hirahara, Real data assimilation for optimization of frictional parameters and prediction of afterslip in the 2003 Tokachi-oki earthquake inferred from slip velocity by an adjoint method, Geophys. J. Int. 203 (1) (2015) 646–663.
[41] F. Massi, Y. Berthier, L. Baillet, Contact surface topography and system dynamics of brake squeal, Wear 265 (11) (2008) 1784–1792.
[42] H. Hetzler, K. Willner, On the influence of contact tribology on brake squeal, Tribol. Int. 46 (1) (2012) 237–246.
[43] D. Tonazzi, F. Massi, L. Baillet, J. Brunetti, Y. Berthier, Interaction between contact behaviour and vibrational response for dry contact system, Mech. Syst. Signal Process. 110 (2018) 110–121.
[44] V. Magnier, J.F. Brunel, P.D. Dufrnoy, Impact of contact stiffness heterogeneities on friction-induced vibration, Int. J. Solid Struct. 51 (9) (2014) 1662–1669.
[45] M. Graf, G.P. Ostermeyer, Instabilities in the sliding of continua with surface inertias: an initiation mechanism for brake noise, J. Sound Vib. 330 (22) (2011) 5269–5279.
[46] M. Graf, G.-P. Ostermeyer, Friction-induced vibration and dynamic friction laws: instability at positive friction-velocity-characteristic, Tribol. Int. 9 (2015) 255–258.
[47] L. Zhang, C. He, Frictional properties of phyllosilicate-rich mylonite and conditions for the brittle-ductile transition, J. Geophys. Res. Solid Earth 121 (4) (2016) 3017–3047.
[48] E. Aharonov, C.H. Scholz, A physics-based rock friction constitutive law: steadystate friction, J. Geophys. Res. Solid Earth 123 (2) (2018) 1591–1614.
[49] M.T. Shaw, W.J. MacKnight, Introduction to Polymer Viscoelasticity, fourth ed., John Wiley & Son, Hoboken, USA, 2018.
[50] J. Woodhouse, S. Wang, The frequency response of dynamic friction: model comparisons, J. Mech. Phys. Solid. 59 (11) (2011) 2294–2306.
[51] R.A. Johnson, D.W. Wichern, Applied Multivariate Statistical Analysis, fourth ed., Prentice-Hall, Upper Saddle River, New Jersey, USA, 1998.
[52] S. Hulikal, K. Bhattacharya, N. Lapusta, Collective behavior of viscoelastic asperities as a model for static and kinetic friction, J. Mech. Phys. Solid. 76 (2015) 144–161.
[53] S. Hulikal, N. Lapusta, K. Bhattacharya, Static and sliding contact of rough surfaces: effect of asperity-scale properties and long-range elastic interactions, J. Mech. Phys. Solid. 116 (2018) 217–238.
[54] J.R. Rice, N. Lapusta, K. Ranjith, Rate and state dependent friction and the stability of sliding between elastically deformable solids, J. Mech. Phys. Solid. 49 (9) (2001) 1865–1898.
[55] S.P. Timoshenko, J.N. Goodier, Theory of Elasticity, third ed., McGraw-Hill, New York, 1970.
[56] R.D. Mindlin, Compliance of elastic bodies in contact, J. Appl. Mech. 16 (1949) 259–268.
[57] J.A. Greenwood, J.B.P. Williamson, Contact of nominally flat surfaces, Philos. Trans. Roy. Soc. A 295 (1442) (1966) 300–319, https://doi.org/10.1098/rspa.1966.0242.
[58] S. Medina, D. Nowell, D. Dini, Analytical and numerical models for tangential stiffness of rough elastic contacts, Tribol. Lett. 49 (1) (2013) 103–115.
[59] R. Pohrt, V. Popov, Contact stiffness of randomly rough surfaces, Sci. Rep. 3 (3293) (2013).
[60] J.R. Rice, A.L. Ruina, Stability of steady frictional slipping, J. Appl. Mech. 50 (2) (1983) 343–349.
[61] T. Putelat, J.H. Dawes, J.R. Willis, Regimes of frictional sliding of a springblock system, J. Mech. Phys. Solid. 58 (1) (2010) 27–53.